Atmos. Meas. Tech., 10, 4537–4560, 2017
https://doi.org/10.5194/amt-10-4537-2017

Atmospheric Measurement Techniques
Open Access
EGU

A new instrument for stable isotope measurements of ^{13}C and ^{18}O in CO_2 – instrument performance and ecological application of the Delta Ray IRIS analyzer

Jelka Braden-Behrens[1], Yuan Yan[1], and Alexander Knohl[1,2]

[1]University of Göttingen, Bioclimatology, Faculty of Forest Sciences and Forest Ecology, Göttingen, Germany
[2]University of Göttingen, Centre of Biodiversity and Sustainable Land Use (CBL), Göttingen, Germany

Correspondence to: Jelka Braden-Behrens (jbraden1@gwdg.de)

Received: 18 April 2017 – Discussion started: 11 May 2017
Revised: 7 September 2017 – Accepted: 13 October 2017 – Published: 24 November 2017

Abstract. We used the recently developed commercially available Delta Ray isotope ratio infrared spectrometer (IRIS) to continuously measure the CO_2 concentration c and its isotopic composition $\delta^{13}C$ and $\delta^{18}O$ in a managed beech forest in central Germany. Our objectives are (a) to characterize the Delta Ray IRIS and evaluate its internal calibration procedure and (b) to quantify the seasonal variability of c, $\delta^{13}C$, $\delta^{18}O$ and the isotopic composition of nighttime net ecosystem CO_2 exchange (respiration) $R^{13}_{eco}C$ and $R^{18}_{eco}O$ derived from Keeling plot intercepts. The analyzer's minimal Allan deviation (as a measure of precision) was below 0.01 ppm for the CO_2 concentration and below 0.03 ‰ for both δ values. The potential accuracy (defined as the 1σ deviation from the respective linear regression that was used for calibration) was approximately 0.45 ppm for c, 0.24 ‰ for ^{13}C and 0.3 ‰ for ^{18}O. For repeated measurements of a target gas in the field, the long-term standard deviation from the mean was 0.3 ppm for c and below 0.3 ‰ for both δ values. We used measurements of nine different inlet heights to evaluate the isotopic compositions of nighttime net ecosystem CO_2 exchange $R^{13}_{eco}C$ and $R^{18}_{eco}O$ in a 3-month measurement campaign in a beech forest in autumn 2015. During this period, an early snow and frost event occurred, coinciding with a change in the observed characteristics of both $R^{13}_{eco}C$ and $R^{18}_{eco}O$. Before the first snow, $R^{13}_{eco}C$ correlated significantly ($p < 10^{-4}$) with time-lagged net radiation R_n, a driver of photosynthesis and photosynthetic discrimination against ^{13}C. This correlation became insignificant ($p > 0.1$) for the period after the first snow, indicating a decoupling of $\delta^{13}C$ of respiration from recent assimilates. For ^{18}O, we measured a decrease of 30 ‰ within 10 days in $R^{18}_{eco}O$ after the snow event, potentially reflecting the influence of ^{18}O depleted snow on soil moisture. This decrease was 10 times larger than the corresponding decrease in $\delta^{18}O$ in ambient CO_2 (below 3 ‰) and took 3 times longer to recover (3 weeks vs. 1 week). In summary, we conclude that (1) the new Delta Ray IRIS with its internal calibration procedure provides an opportunity to precisely and accurately measure c, $\delta^{13}C$ and $\delta^{18}O$ at field sites and (2) even short snow or frost events might have strong effects on the isotopic composition (in particular ^{18}O) of CO_2 exchange on an ecosystem scale.

1 Introduction

The stable isotopic compositions of CO_2 and water vapor have been intensely used to study ecosystem gas exchange (Yakir and Sternberg, 2000). In particular, measurements of the $\delta^{13}C$ and $\delta^{18}O$ isotopic composition of CO_2 have provided important insights into the carbon cycle over a large variety of spatial and temporal scales (Flanagan and Ehleringer, 1998; Affek and Yakir, 2014). There are many examples for the utility of the stable isotopic composition of CO_2 to study biosphere–atmosphere exchange processes on an ecosystem scale, such as the partitioning of net ecosystem CO_2 exchange into respiration and photosynthesis. Different partitioning methods include the combination of gra-

dient approaches with stable isotope measurements (Yakir and Wang, 1996), direct isotope gradient approaches (Zhang et al., 2006), the combination of eddy covariance measurements with isotope flask measurements (Bowling et al., 2001; Ogée et al., 2003; Knohl and Buchmann, 2005) and direct isotope eddy covariance measurements (Wehr et al., 2016; Oikawa et al., 2017). Other field applications of stable CO_2 isotopes measurements investigate the temporal variability of the isotopic composition of a particular flux component. The temporal variability of the isotopic composition of respiration for example has been studied on timescales ranging from sub-diurnal (Barbour et al., 2011) to seasonal (Ekblad and Högberg, 2001; Bowling et al., 2002; Knohl et al., 2005). Further, the isotopic composition in CO_2 profiles has been studied on several sites over multiple years for ^{13}C (e.g., Bowling et al., 2002; Wehr et al., 2016) as well as for ^{18}O (e.g., Bowling et al., 2003b; Shim et al., 2013). The ^{13}C composition of ecosystem respiration $R^{13}_{eco}C$, on the one hand, has been used to assess the time lag between assimilation and respiration (Ekblad and Högberg, 2001; Bowling et al., 2002; Knohl et al., 2005) and to evaluate biosphere models on a global scale (Ballantyne et al., 2011). The ^{18}O composition of ecosystem CO_2 exchange $R^{18}_{eco}O$, on the other hand, is particularly interesting for studying the coupled CO_2 and water cycle (see e.g., Yakir and Wang, 1996).

A long-established and broadly used technique to measure stable isotopic compositions is isotope ratio mass spectrometry (IRMS; Griffis, 2013), a technique that is based on the fact that moving ions with different mass-to-charge ratios can be separated by (orthogonal) magnetic fields (Thomson, 1908). For measurements of the isotopic composition of CO_2, IRMS has typical precisions of approximately 0.02 to 0.1 ‰ for ^{13}C and 0.05 to 0.2 ‰ for ^{18}O. IRMS has been widely used for isotope studies in environmental sciences, though it shows limited applicability for in situ measurements (Griffis, 2013), but see also the field-applicable continuous flow IRMS described by Schnyder et al. (2004). Disadvantages of flask-sampling-based IRMS techniques include high sample preparation effort and costs (Griffis, 2013), low temporal resolution and discontinuous measurements. Additionally, there are potential problems during sample storage and transport, see Knohl et al. (2004) for minimizing such storage effects in the case of ^{13}C. For ^{18}O, storage effects can be related to oxygen exchange between water and CO_2 (Gemery et al., 1996; Tuzson et al., 2008). Optical-based techniques can compete with or complement IRMS measurements, and progress in optical-based techniques over the last decade has enhanced the potential of measurements of isotopic compositions (Werner et al., 2012). These developments have a particular impact on micrometeorological studies, as they increased the accessibility of field-deployable optical instruments and thus enabled a number of micrometeorological applications of stable isotope techniques, as reviewed by Griffis (2013). Optical instruments to study the isotopic composition of trace gases use the absorption of infrared photons

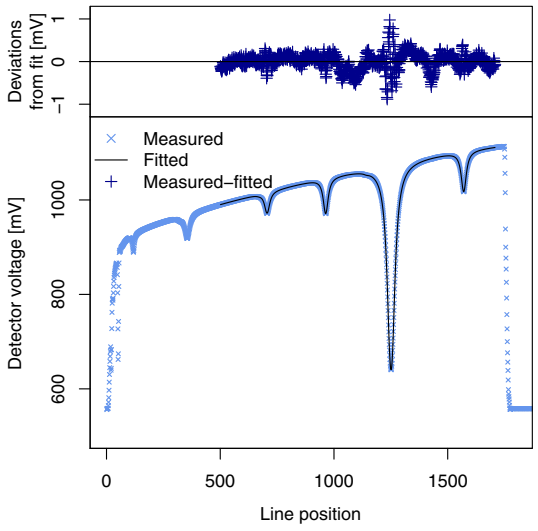

Figure 1. Measured and fitted spectrum, as exported from the instrument's operational software Qtegra.

by exciting a molecule's rotational and vibrational energy states. These rotational and vibrational transitions are characteristically different for isotopologues, defined, for example, by Coplen (2011) as "molecular species that differ only in isotopic composition" (see e.g., Esler et al., 2000; Kerstel and Gianfrani, 2008)[1]. The isotopologue-specific absorption lines are related to the concentration of the respective isotopologue via Beer's law and thus the isotopic composition of a certain molecule (Werle, 2004). Available optical instruments that are capable of measuring isotopic compositions at trace gas concentrations show different implementations of this principle by using different light sources (broadband light sources, mid- or near-infrared lasers) (see e.g., Griffis, 2013; Kerstel and Gianfrani, 2008) and/or different absorption cells (multipath or resonant) (Werle, 2004). Minimal Allan deviations σ_A and the corresponding averaging times τ_{min} for different optical instruments are shown in Table 2, but see also Table 2 in the review of Griffis (2013) for more detailed information, including instrument stability and an overview of applications, for most of these instruments.

Here we present a new laser-based direct absorption spectrometer in the mid-infrared, the isotope ratio infrared spectrometer (IRIS) Delta Ray (Thermo Scientific Inc., Waltham, USA). This spectrometer uses two tunable near-infrared diode lasers in combination with a nonlinear crystal to produce a laser beam in the mid-infrared (Thermo Fisher Scientific, 2014). The instrument scans a spectral region from 4.3293 to 4.3275 µm, containing four CO_2 absorption lines: at 4.3277 and 4.3280 µm (both for $^{16}O^{12}C^{16}O$), 4.3283 µm

[1] In general this is also true for isotopomers, defined, for example, by Coplen (2011) as "molecular species having the same number of each isotopic atom [. . .] but differing in their positions" (e.g., Mohn et al., 2008).

Table 1. Nomenclature and abbreviations used in this publication; numbers for reference standards R_{std} from International Atomic Energy Agency (1995).

Stable-isotope-specific nomenclature	
R_{std}	Isotope ratio C_{heavy}/C_{light} of an (arbitrary) reference standard
δ value	Relative deviation of the measured isotope ratio from R_{std}
VPDB	Vienna Pee Dee Belemnite – standard for ^{13}C ($R_{VPDB} \approx 0.01124$)
VPDB-CO_2	Vienna Pee Dee Belemnite – standard for ^{18}O ($R_{VPDB-CO2} \approx 0.0020883$)
Nomenclature	
σ_A	Allan deviation
R_n	Net radiation
RH	Relative humidity
VPD	Vapor pressure deficit
δ_{KP}	Keeling plot intercept
R_{eco}	Isotopic composition of nighttime CO_2 exchange (respiration) integrated over the ecosystem
Technical abbreviations	
IRIS	Isotope ratio infrared spectrometer
IRMS	Isotope ratio mass spectrometer
OA-ICOS	Off-axis integrated cavity output spectroscopy
CRDS	Cavity ring-down spectroscopy

(for $^{16}O^{13}C^{16}O$) and 4.3286 µm (for $^{16}O^{12}C^{18}O$) (Geldern et al., 2014). A measured and a fitted spectrum is shown in Fig. 1. The fitting procedure is based on a Voigt profile fit that relates the isotopologue-specific absorption lines to their respective concentrations (information from the manufacturer, Thermo Fisher Scientific). The instrument has a flow rate of 0.08 slpm, a cell pressure of approximately 100 mbar, an optical path length of approximately 5 m, and an internal calibration procedure that automatically includes two point calibrations for concentration c and both δ values as well as corrections for the concentration dependency of the measured δ values (Thermo Fisher Scientific, 2014). The objectives of our study are (a) to characterize the Delta Ray IRIS and its performance under field conditions as well as (b) to quantify the seasonal variability of $\delta^{13}C$, $\delta^{18}O$ and the isotopic composition of CO_2 exchange for both $\delta^{13}C$ and $\delta^{18}O$ derived from Keeling plot intercepts.

2 Material and methods

2.1 Field site

This study was conducted at a meteorological tower in a managed beech forest (*Fagus sylvatica L.*) in Thuringia (central Germany) at 51°19′41,58″ N; 10°22′04,08″ E at 450 m above sea level. The forest in the dominant wind direction of the tower has an average canopy height of approximately 34 m with approximately 120-year-old trees, a top-weighted canopy and a homogeneous stand structure, surrounded by trees of three age classes (approximately 30–40, 80 and 160 years; Anthoni et al., 2004). The field site is described in detail by Anthoni et al. (2004), and soil characteristics of this site were analyzed by Mund (2004).

2.2 Campaign design

We measured the CO_2 concentration c and its isotopic composition $\delta^{13}C$ and $\delta^{18}O$ in ambient air from 21 August to 16 November 2015. We measured these quantities with the field deployable isotope ratio infrared spectrometer Delta Ray (Thermo Scientific, Waltham, USA) at nine inlet heights ranging from 0.1 to 45 m in an automatic measurement setup. After the tubing was purged for 60 s, each inlet was measured for 80 s (consisting of four measurements each averaged for 20 s – thus, the averaging time is longer than the instrument internal cell response time $\tau_{10\,\%}$; see Sect. 3.1.4). A full measurement cycle took 30 min and consisted of measurements of all nine inlet heights and a target standard with known CO_2 concentration and isotopic composition (CO_2 in synthetic air, tank SA-CO_2-5 in Table 3), supplemented by an internal calibration measurement, called "referencing" (see Sect. 2.8). In less detail, the experimental setup is also described in Braden-Behrens et al. (2017).

We used the nighttime measurements of c, $\delta^{13}C$ and $\delta^{18}O$ of the different inlet heights in a Keeling plot approach (Keeling, 1958) to calculate the nighttime Keeling plot intercept that can be used to estimate the isotopic composition of nighttime net ecosystem CO_2 exchange (respiration) δR_{eco} for both measured δ values: ^{13}C and ^{18}O. Additionally, we used the half-hourly measurements of the target standard to track the repeatability of the Delta Ray analyzer and

Table 2. Examples for different optical instruments that measure the isotopic composition of CO_2 and reported values for minimal Allan deviations σ_A and the corresponding averaging times τ_{min} (if available), see also Table 2 of the review of Griffis (2013).

Broadband-light-source-based instruments	
Instrument	Fourier-transform infrared spectrometer: Spectronus analyzer (Ecotech Pty Ltd., Australia)
Minimal Allan deviation for $\delta^{13}C$	$\sigma_A(\tau_{min} \approx 6000\,s) = 0.01\,‰$ (Griffith et al., 2012)
Minimal Allan deviation for $\delta^{18}O$	$\sigma_A(\tau_{min} \approx 7200\,s) = 0.1\,‰$ (Vardag et al., 2015)
Instrument	Fourier-transform infrared spectrometer: Nicolet Avatar (Thermo Electron, USA)
Minimal Allan deviation for $\delta^{13}C$	$\sigma_A(\tau_{min} \approx 960\,s) = 0.15\,‰$ (Mohn et al., 2007)
Laser-based direct absorption spectrometers in mid-infrared	
Instrument	Quantum cascade laser absorption spectrometer: QCLAS (Aerodyne Research Inc., USA)
Minimal Allan deviation for $\delta^{13}C$	$\sigma_A(\tau_{min} \approx 100\,s) = 0.01\,‰$ (Wehr et al., 2013); $\sigma_A(\tau_{min} \approx 100\,s)$=0.06 ‰ (Sturm et al., 2012)
Minimal Allan deviation for $\delta^{18}O$	$\sigma_A(\tau_{min} \approx 100\,s) = 0.06\,‰$ (Sturm et al., 2012)
Instrument	Lead–salt tunable diode laser absorption spectrometer: TGA100A/200 (Campbell Scientific Inc., USA)
Minimal Allan deviation	No data for uncalibrated minimal σ_A, ideal averaging time $\tau_{min} \approx 30\,s$ (Bowling et al., 2003c)
High-frequency Allan deviation	$\sigma_A\ (\tau = 0.1\,s) = 1.5\,‰$ for $\delta^{13}C$ and 2.2 ‰ for $\delta^{18}O$ (Bowling et al., 2003c)
Instrument	Isotope ratio infrared spectrometer: Delta Ray (Thermo Scientific Inc., USA)
Minimal Allan deviation for $\delta^{13}C$	$\sigma_A(\tau_{min} \approx 500\,s) = 0.04\,‰$ (Geldern et al., 2014); $\sigma_A(\tau_{min} \approx 300\,s) = 0.02$ ‰ (this study, Table 5)
Minimal Allan deviation for $\delta^{18}O$	$\sigma_A(\tau_{min} \approx 300\,s) = 0.04\,‰$ (this study, Table 5)
Laser-based path-length-enhanced absorption spectrometers in near infrared	
Instrument	Cavity ring-down spectrometer: G1101-i+ (Picarro Inc., USA)
Minimal Allan deviation for $\delta^{13}C$	$\sigma_A(\tau_{min} \approx 3600\,s) \leq 0.1\,‰$ (Vogel et al., 2013)
Instrument	Off-axis integrated cavity output spectrometer: CCIA DLT-100 (Los Gatos Research Inc., USA)
Minimal Allan deviation for $\delta^{13}C$	$\sigma_A(\tau_{min} \approx 200\,s) = 0.04\,‰$ (at approximately 20 000 ppm CO_2; Guillon et al., 2012); $\sigma_A(\tau_{min} \approx 200\,s) = 0.6\,‰$ (at approximately 2 000 ppm CO_2; Guillon et al., 2012)
Laser-based path-length-enhanced absorption spectrometers in mid-infrared	
Instrument	Quantum cascade laser absorption spectrometer: CCIA-48 (Los Gatos Research Inc., USA)
Minimal Allan deviation for $\delta^{13}C$	$\sigma_A(\tau_{min} \approx 300\,s) = 0.06\,‰$ (Oikawa et al., 2017)
Minimal Allan deviation for $\delta^{18}O$	$\sigma_A(\tau_{min} \approx 300\,s) = 0.04\,‰$ (Oikawa et al., 2017)

performed additional (manual) measurements to characterize the analyzer.

2.3 Spectrometer setup

We set up the spectrometer to use the absorption lines at 4.3277 µm (for $^{16}O^{12}C^{16}O$), 4.3283 µm (for $^{16}O^{13}C^{16}O$) and 4.3286 µm (for $^{18}O^{12}C^{16}O$). Thus, only three of the four absorption lines in the instrument's measured spectra (Fig. 1) were used for the spectral fit. In particular, for $^{16}O^{12}C^{16}O$, we did not use the strong absorption line at 4.3280 µm. The corresponding mode of operation is called "high-concentration mode" in the instrument's operational software Qtegra. Additionally, the sample was dried before it entered the measurement cell with the (instrument's internal) Nafion drier.

2.4 Application of the Keeling plot approach

The Keeling plot approach (Keeling, 1958) is based on a simple two-component mixing model that describes how air from a source with effectively constant isotopic composition δ_s mixes with a background (with constant c_{bg} and δ_{bg}). For this simple two-component mixing model, one can derive a linear relationship between the measured isotopic composition δ_{meas} and the reciprocal concentration $1/c_{meas}$ by applying conservation of mass for the total concentration as well as for each isotopologue separately (for derivation see e.g., Pataki et al., 2003).

$$\delta_{meas} = \underbrace{(\delta_{bg} - \delta_s)\, c_{bg}}_{m_{KP}} \frac{1}{c_{meas}} + \underbrace{\delta_s}_{\delta_{KP}} \quad (1)$$

This linear relationship with slope m_{KP} and intercept δ_{KP} can be derived for each isotopic species independently, so in our case for both $\delta^{13}C$ or $\delta^{18}O$. The applicability of the Keel-

Table 3. Known CO_2 concentrations c and δ values for gas tanks used for calibration and instrument performance measurements. All measured concentrations and δ values refer to measurements that were performed at the Max Planck Institute for Biogeochemistry in Jena and the $\delta^{13}C$ values of the two pure CO_2 tanks. The pure CO_2 tanks bio and ambient were additionally measured with IRMS at the Geoscience Center in Göttingen (Isotope Geology Division, Göttingen University) for their ^{13}C composition. Abbreviations for the purpose of the tanks: cCAL, concentration calibration; dCAL, δ calibration; REF, referencing; EC, evaluating calibration; pcCAL, post-concentration calibration; REP, repeatability measurement.

Gas tank	Used for	c (ppm)	$\delta^{13}C$ (‰VPDB)	$\delta^{18}O$ (‰VPDB-CO_2)
Pure CO_2 (ambient)	dCAL, REF, EC	–	-9.94 ± 0.01	-17.5 ± 0.3
Pure CO_2 (bio)	dCAL, EC	–	-28.25 ± 0.01	-27.2 ± 0.3
Pure CO_2 (bio2)	EC	–	-26.1 ± 0.3	-24.3 ± 0.3
Pressurized air (PA-tank)	pcCAL, EC	413.7 ± 0.2	-9.7 ± 0.2	-5.3 ± 0.4
Synthetic air with CO_2 (SA-CO_2-1)	cCAL, pcCAL, EC	349.5 ± 0.1	-37.01 ± 0.02	-34.1 ± 0.4
Synthetic air with CO_2 (SA-CO_2-2)	cCAL, pcCAL	453.9 ± 0.1	-36.98 ± 0.02	-34.2 ± 0.6
Synthetic air with CO_2 (SA-CO_2-3)	pcCAL	349.6 ± 0.1	-37.02 ± 0.01	-34.3 ± 0.4
Synthetic air with CO_2 (SA-CO_2-4)	pcCAL, EC	453.2 ± 0.1	-37.02 ± 0.02	-34.8 ± 0.4
Synthetic air with CO_2 (SA-CO_2-5)	pcCAL, REP	396.5 ± 0.1	-37.02 ± 0.02	-34.7 ± 0.2
Synthetic air with CO_2 (SA-CO_2-6)	EC	496.0 ± 0.1	-37.02 ± 0.02	-34.8 ± 0.1

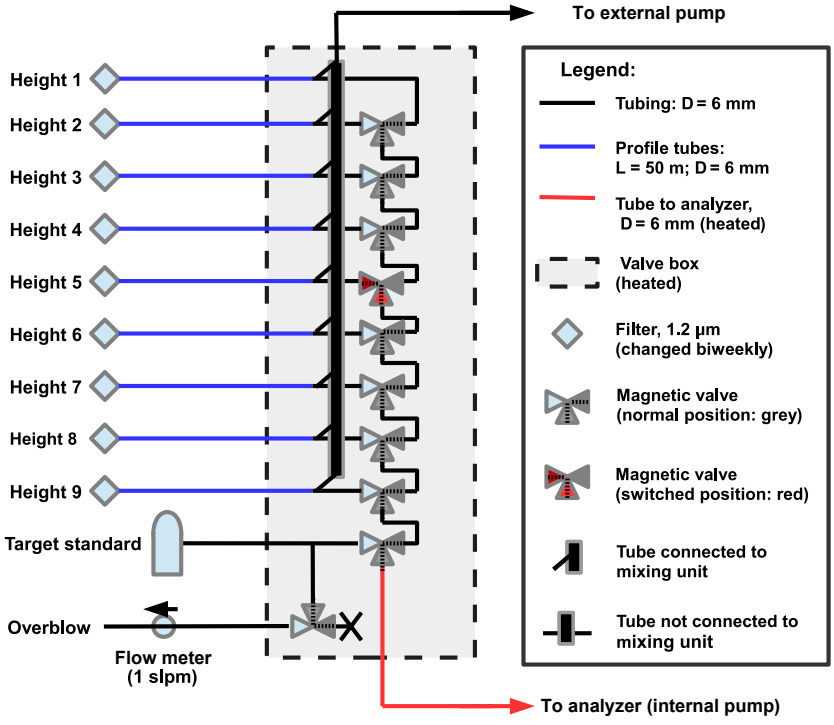

Figure 2. Plumbing scheme for the measurements of nine heights and a target standards; the example shows the valve positions when height 5 is sampled.

ing plot approach to a certain experimental setup essentially depends on the question of whether c_{bg}, δ_{bg} and δ_s are constant over the spatial and temporal distribution of all measurements that are taken into account for the linear regression. In this study we apply a Keeling plot approach to a forest ecosystem, aiming at measuring the isotopic composition of ecosystem-integrated CO_2 exchange. The source of CO_2 is thus composed of different individual source components i (e.g., stem, leaf and soil respiration), with each accounting for the individual components with their isotopic compositions $\delta_{s,i}$. The corresponding isotopic composition of the integrated source δ_s can be expressed by defining α_i as the relative contributions of the individual source components to

the integrated source.

$$\delta_s = \sum_i \delta_{s,i}\ \alpha_i \qquad \text{with} \qquad \sum_i \alpha_i = 1 \tag{2}$$

If the relative distributions among the different source components α_i produce significant changes in δ_s over the spatial and temporal distribution of measurements, the basic two-component assumption of stable δ_s is violated. During daytime the application of a Keeling plot approach on an ecosystem scale in a forest is in general problematic, as photosynthesis and respiration are two separately controlled and spatially separated processes – so we generally cannot assume spatiotemporally constant α_i. However, for nighttime, when there is only respiration, the nighttime Keeling plot intercept δ_{KP} can be interpreted as the isotopic composition of nighttime net ecosystem CO_2 exchange (respiration) $\delta^{13}C\ R_{eco}$ or $\delta^{18}O\ R_{eco}$. Measures to assure and test the applicability of this two-component approach and to improve the quality of the calculated Keeling plot intercepts are discussed and evaluated in Appendix A. In brief, they include the minimization of the sampling time for each Keeling plot, an inclusion of all inlet heights into each Keeling plot analysis to increase the CO_2 concentration range, data filtering and weighted averaging of Keeling plots on smaller timescales.

2.5 Material and technical specifications

Technical specifications of the setup including plumbing and the automatic switching unit are shown schematically in Fig. 2. The automatic switching unit consisted of 10 electromagnetic 3/2-way valves (Fig. 2) and was operated by a PC using software for measuring technology (ProfiLab Expert 4.0, Abacom, Germany). The operating software controlled the valve positions using two USB relay boards (Abacom, Germany). When switching the valves to a new position, the operating software additionally sent a 1 s long rectangular trigger pulse with 5 V DC to one of the Delta Ray analyzer's two different analogue input channels. One of these channels was used when a target gas measurement had to be started, whereas a trigger pulse at the other input channel initialized the height measurements. After the Delta Ray analyzer received one of the trigger pulses, the tubes and the measurement cell were purged for 60 s before the analyzer took measurements for 80 s. This purging time was used to ensure that the first measurement after switching contained less than 0.1 % of the previously measured sample (see Sect. 3.1.4).

We used polyethylene (PE) tubes with 6 mm outer diameter and 4 mm inner diameter (Landefeld GmbH, Kassel, Germany) for the plumbing in the switching unit as well as for the nine height inlets. These inlets were additionally equipped with 1.2 µm PTFE (polytetrafluoroethylene) membrane filters replaced every 2 weeks (Rettberg GmbH, Göttingen, Germany). The tubes for the nine height inlets (see Fig. 2) were all equally long (50 m) – except for the highest inlet that had to be extended to 52 m for practical reasons. The equal (or similar) length of the inlet tubes lead to similar flow rates in the tubing system and similar inlet pressures for the analyzer regardless of the valve position. This decreased pressure jumps when switching from one height position to another. We purged the main tube to reduce the time the air masses spend in the tubing. To avoid condensation, we heated the valve box (at which we expected a pressure drop) and the adjacent tubing. For heating we used self-regulating heating wires (Horst GmbH, Lorsch, Germany) which produce a constant temperature of 65 °C. The flow rate in the height inlet tubes was approximately 1.5 slpm for all heights all the time and the major part of the gas flow was directed into the purging pump. In the case of the target standard, the tubing was only purged when the target standard was measured. In this case, an overblow opened to enable gas release at approximately 1 slpm (Fig. 2). For the target measurements as well as for the height measurements the analyzer took a subsample of the corresponding inlet line with a flow rate of approximately 0.08 slpm. The flow in all the tubing was laminar with Reynolds numbers below 100.

For measurements as well as calibration, we used gas tanks in 50 L steel containers at 150 to 200 bar pressure containing synthetic air, synthetic air with different CO_2 concentrations and pressurized air (Westfalen AG, Gleichen, Germany). Additionally, we used three 1 L gas tanks at 10 bar pressure with pure CO_2 at different (known) δ values that were shipped with the Delta Ray analyzer (Air Liquide, Düsseldorf, Germany). All used CO_2-containing gas tanks were measured high precisely for their CO_2 concentration and isotopic composition in ^{13}C and ^{18}O at the Max Planck Institute (MPI) for Biogeochemistry in Jena. There, the CO_2 concentrations were measured with a Picarro CRDS G1301 and the isotopic composition was measured with IRMS linked to VPDB (VPDP-CO_2) by using the multipoint scale anchor JRA-S06 (Wendeberg et al., 2013). The pure CO_2 tanks that were used for δ calibration were additionally measured for their ^{13}C composition with IRMS at the Geoscience Center in Göttingen (Isotope Geology Division, Göttingen University). All known δ values and concentrations for the gas tanks used in this application can be found in Table 3 with their corresponding uncertainties.

2.6 Instrument characterization measurements

We carried out additional measurements in the field and in the lab to quantify precision, evaluate the calibration strategy, and quantify the instrument's response time and repeatability. These measurements involved changes in the analyzers plumbing. For all measurements that required connecting different gas tanks to the analyzer, they were either connected directly to the analyzer's internal ports (Ref1, Ref2, CRef1 and CRef2) or the plumbing was equivalent to the plumbing of the target gas (Fig. 2).

1. Lab measurements to quantify precision and evaluate the calibration strategy.
   - We measured the Allan deviation by connecting pressurized air at atmospheric δ values to the analyzer and took measurements at the analyzer's maximum data acquisition rate of 1 Hz for 2 h.
   - We diluted pure CO_2 with synthetic air over a CO_2 concentration range of 200 to 1500 ppm to measure the concentration dependency of the measured (raw) δ values. This dilution experiment was carried out for three different tanks with pure CO_2 at different δ values. Each gas tank was measured twice. (Used gas tanks: ambient, bio and bio2; see Table 3).
   - We measured the concentration c and the isotopic compositions $\delta^{13}C$ and $\delta^{18}O$ of gases with concentrations ranging from 350 to 500 ppm and isotopic compositions ranging from -37 to $-9.7\,‰$ for $\delta^{13}C$ and from -35 to $-5\,‰$ for $\delta^{18}O$. Each of these measurements was performed three times. (Used gas tanks: ambient, bio, bio2, PA-tank, SA-CO_2-1, SA-CO_2-4, SA-CO_2-6; see Table 3).
   - We carried out repeated measurements of two pure CO_2 gas tanks at different δ values (diluted to different concentrations between 200 and 3000 ppm) as well as measurements of two gas tanks at different CO_2 concentrations (350 and 500 ppm). These measurements were repeated every 6 h for a period of 9 days. (Used gas tanks: ambient, bio, SA-CO_2-1 and SA-CO_2-6; see Table 3.)
2. Field measurements to quantify the setup's response time and repeatability.
   - The response time of the tubing and the analyzer was measured by using the automatic switching unit (Fig. 2) to switch from ambient air (height 9) to the target standard. We superimposed the measurements of four switching events to observe the adjacent temporal response processes.
   - The analyzer's repeatability under field conditions was quantified by the half-hourly target measurements described in Sect. 2.5

2.7 Meteorological measurements

Supplementary to the measurements with the Delta Ray analyzer, the meteorological tower at the field site is equipped with an eddy covariance system to measure CO_2 and H_2O_v fluxes as well as latent and sensible heat fluxes. Additional standard meteorological measurements include continuous measurements of shortwave and longwave radiation, wind speed and direction, precipitation, air and soil temperature, and air and soil humidity (Anthoni et al., 2004).

2.8 Calibration

2.8.1 Instrument internal calibration

The Delta Ray analyzer is equipped with three different internal calibration routines (Thermo Fisher Scientific, 2014). We performed these routines at the field site (in situ) each time the analyzer had to be restarted, for example, after power supply failures, instrument issues or when we manually turned off the analyzer for other reasons. All three instrument internal calibration procedures were usually done 1 day after restarting the analyzer; thus, the instrument was in thermal equilibrium during calibration. The three different instrument internal calibration procedures are described below.

- *Correction of concentration dependency.* This correction is called "linearity calibration" in the instrument's documentation and operational software. The calibration routine evaluates the concentration dependency of δ-value measurements (Thermo Fisher Scientific, 2014). Mathematically, an experimentally derived correction factor f_{correct} (c_{raw}) is multiplied with the raw isotopic ratio R (information from the manufacturer, Thermo Fisher Scientific):

$$R_{c\text{-corrected}} = f_{\text{correct}}(c_{\text{raw}}) \times R_{\text{raw}}. \quad (3)$$

  This factor as a function of concentration is determined via a natural spline fit of measurements of a gas tank with constant δ value at different concentrations (information from the manufacturer, Thermo Fisher Scientific). This is implemented by mixing pure CO_2 with CO_2-free air, yielding concentrations between 200 and 3500 ppm. In our setup we used the pure CO_2 with near-to-ambient δ values (ambient tank, see Table 3) and synthetic air for this calibration.
- *Delta scale calibration.* This calibration routine is based on a two-point calibration of δ values using two tanks of pure CO_2 with different δ values that are diluted with synthetic air. For this calibration, we used the pure CO_2 tanks ambient and bio (see Table 3).
- *Concentration calibration.* This calibration routine performs a two-point calibration for CO_2 concentration using two gas tanks with different CO_2 concentrations. We performed this measurement simultaneously to the other two calibration routines in the field, but for one particular calibration on 15 October, we had to replace it by a post-calibration, which is described in Sect. 2.8.2.

The instrument's internal calibration procedure is based on the measurement of these calibration curves after the instrument is started in combination with repeated measurements of a known gas, so-called "referencing" (see below). As the

different calibrations are only performed once after the instrument is restarted, the accuracy and repeatability of measurements is further based on the assumption that these relationships remain sufficiently constant, and temporal changes are corrected by "referencing".

– *Referencing.* This procedure applies an offset correction of the calibrated δ values using a gas with known δ values that is measured at a freely selectable concentration at regular intervals (information from the manufacturer, Thermo Fisher Scientific). In our experimental setup, referencing is carried out every 30 min for 80 s after the tubes have been purged for 60 s using the pure CO_2 standard (ambient, see Table 3) diluted with synthetic air. We chose the reference concentration to be the same as the concentration at the highest inlet in the adjacent measurement cycle, because most of the measurement inlets had concentrations close to those at the highest inlet and the temporal variability of the measured concentrations generally decreased with height. Thus, we performed the "referencing" as close as possible to as many height measurements as possible by using these settings.

Thus, the calibration procedure for δ values can be expressed with the following formula with the correction factor $f_{\mathrm{correct}}(c_{\mathrm{raw}})$ as determined from the concentration-dependency correction and the slope $m_{\delta\mathrm{scale}}$ derived from the δ scale calibration (information from the manufacturer, Thermo Fisher Scientific).

$$\delta_{\mathrm{calibrated}}(R_{\mathrm{raw}}; c_{\mathrm{raw}}; t) = m_{\delta\mathrm{scale}} \times \underbrace{\left(\frac{f_{\mathrm{correct}}(c_{\mathrm{raw}})R_{\mathrm{raw}}}{R_{\mathrm{std}}} - 1\right)}_{\delta_{c\text{-corrected}}(c_{\mathrm{raw}})} + \delta_{\mathrm{Offset}}(t) \quad (4)$$

2.8.2 Post-processing for concentration calibration

For the time period from 15 October to 15 November, we replaced the instrument's internal concentration calibration by a manual linear calibration, based on manual measurements with six different gas tanks in the field. This was necessary, because measurements with these different gas tanks (including the target standard) showed a consistent linear relationship between raw and known concentrations that deviated from the linear relationship that was used in the instrument's internal calibration. Thus, we conclude that during this period there was a problem with the instrument's internal concentration calibration which might be related to gas flow or a leak during this particular concentration calibration.

2.9 Multilayer modeling

To test if the measured variability of the ^{13}C composition of respiration can be partly explained by the variability of the ^{13}C composition of recent assimilates, we used the multilayer model CANVEG to simulate the isotopic composition of assimilated material during our measurement campaign. In particular, we analyzed the correlation of modeled $^{13}C_{\mathrm{Ass}}$ to net radiation R_{n}, a driver of photosynthesis and photosynthetic discrimination, during our measurement period in autumn 2015. We further compared the resulting relationship between R_{n} and $^{13}C_{\mathrm{Ass}}$ to the observed (time lagged) relationship between R_{n} and the ^{13}C composition of ecosystem respiration $R^{13}_{\mathrm{eco}}C$, derived from the measured Keeling plots (see Sect. 3.2.2). This analysis was performed to test the hypotheses of a link between δ values in assimilated material and respiration. We used the multilayer model CANVEG to calculate the isotopic composition of assimilated material $\delta^{13}C_{\mathrm{Ass}}$. CANVEG is a biophysical one-dimensional multilayer canopy model (see e.g., Baldocchi, 1997; Baldocchi and Wilson, 2001). This multilayer model uses hourly meteorological inputs (among others, temperature, radiation, vapor pressure deficit [VPD], wind velocity and CO_2 concentration) as main drivers, as well as site-specific parameters (leaf area index, leaf clumping status, canopy height, etc.). Based on these input variables, CANVEG iteratively computes the biosphere–atmosphere exchange of water, carbon dioxide and energy as well as the microclimate within and above the canopy at hourly time steps. The carbon, water and energy modules have been validated for various environmental conditions and forest types (see e.g., Baldocchi et al., 1997, 1999, 2002). In particular, the model has also been applied to an unmanaged beech-dominated forest field site at an approximately 30 km air-line distance to the measurement site of this study (Knohl and Baldocchi, 2008).

Table 4. Validation of the multilayer model CANVEG using eddy covariance measurements of gross primary productivity (GPP), net ecosystem exchange (NEE), and latent and sensible heat flux (LE and H). Slopes, R^2 values and normalized standard error estimates (NSEE) of linear regressions between modeled and measured values are comparable to the numbers given by Knohl and Baldocchi (2008).

	SLOPE	R^2	NSEE
GPP	0.92	0.90	0.26
NEE	0.97	0.92	0.28
LE	1.03	0.78	0.16
H	0.96	0.87	0.37

The isotope-enabled version of this model additionally calculates $\delta^{13}C_{ij}$, the ^{13}C composition of CO_2 for each canopy layer i and each hourly time step j, and the corresponding ^{13}C composition of assimilated material $\delta^{13}C_{\mathrm{Ass},ij}$ (Baldocchi and Bowling, 2003). In our application, we set up the model to use 40 equally thick layers i and we used our meteorological measurements at the field site, described in Sect. 2.7, as input variables. We validated the model with eddy covariance measurements (Table 4) and used the model

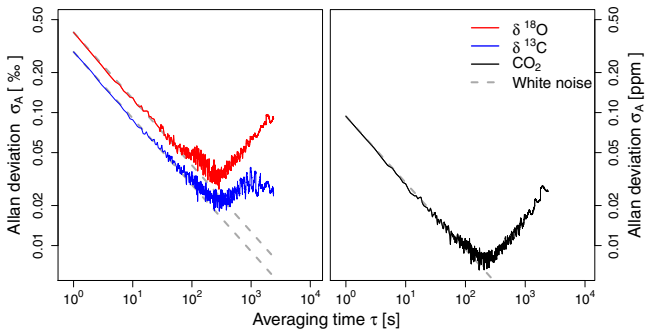

Figure 3. Allan deviation σ_A in ‰ VPDB for ^{13}C, in ‰VPDB-CO_2 for ^{18}O and in ppm for CO_2 concentration; solid lines show the calculated Allan deviation and dashed lines show the typical white frequency noise error scaling.

to calculate the isotopic composition of assimilated material $\delta^{13}C_{Ass,ij}$ for each of the 40 canopy layers i and for each hourly time step j. The ^{13}C composition of assimilated material $\delta^{13}C_{Ass}$ on a daily timescale was calculated as an assimilation-weighted sum over all layers and time steps, with the modeled assimilation rate A_{ij} as a weighting factor:

$$\delta^{13}C_{Ass} = \frac{\sum_{i=1}^{40}\sum_{j=1}^{24} A_{ij} \cdot \delta^{13}C_{Ass,ij}}{\sum_{i=1}^{40}\sum_{j=1}^{24} A_{ij}}. \quad (5)$$

We included only hours j and layers i during photosynthesis (with positive assimilation rates).

3 Results and discussion

3.1 Instrument characteristics

3.1.1 Precision

We use the Allan deviation σ_A at different averaging times τ (Table 5) to characterize the Delta Ray IRIS analyzer's precision. Starting at an averaging time of 1 s that corresponds to the analyzer's maximum data acquisition frequency, the Allan deviation σ_A decreased with $\tau^{-1/2}$ (Fig. 3). This matches the expected behavior of a system that is dominated by white frequency noise. The measured Allan deviation σ_A followed this slope up to averaging times for approximately 300 s for δ-value measurements and approximately 200 s for concentration measurements. At these timescales the analyzer showed its maximum precision of 0.02 ‰ VPDB for $\delta^{13}C$, 0.03 ‰ VPDB-CO_2 for $\delta^{18}O$ and 0.007 ppm for CO_2 concentration. For averaging times above 200–300 s other error sources (such as instrument drift) became significant. For $\delta^{13}C$, the precision of an earlier version of the instrument has also been measured by Geldern et al. (2014), reporting a minimum of σ_A at around 0.04 ‰ for an averaging time of $\tau \approx 550$ s. At this averaging time, we measured a comparable (slightly better) Allan deviation below 0.03 ‰ (see Table 5). Two other averaging times are particularly interesting for our application: firstly, the averaging period of 20 s yields Allan variances below 0.1 ‰ for both δ values and 0.02 ppm for CO_2 concentration; secondly, we set the IRIS analyzer's internal referencing procedure (described in Sect. 2.8) to 1800 s, which corresponds to an Allan variance of 0.03 ‰ for $\delta^{13}C$ and 0.08 ‰ for $\delta^{18}O$ values and 0.01 ppm for CO_2 concentration.

Table 5. Allan deviation σ_A for different averaging times τ, with the minimum Allan deviation for $\tau_{min} \approx 290 s$ for both δ values and 170 s for CO_2 concentration c

τ (s)	$\delta^{13}C$ (‰)	$\delta^{18}O$ (‰)	c (ppm)
1	0.29	0.40	0.09
20	0.06	0.09	0.02
80	0.03	0.05	0.02
τ_{min}	0.02	0.03	0.007
500	0.03	0.04	0.01
1800	0.03	0.08	0.01

3.1.2 Evaluation of the calibration strategy

The instrument's internal calibration strategy (described in Sect. 2.8) is based on the following:

- A nonlinear relationship between raw δ values and concentrations (Fig. 4).
- A linear relationship between the calibrated δ value (measured with IRMS) and the concentration-corrected δ value ($\delta_{c\text{-corrected}}$ in Eq. 4) (Fig. 5, middle and right panel).
- A linear relationship between measured (raw) and real concentrations (Fig. 5, left panel).
- The repeatability of the calibration curves – for δ values modulo the offset correction that is applied by the instrument's internal "referencing" (Fig. 6 and Table 7).

Raw δ values show a nonlinear dependency from raw concentrations (Fig. 4). This nonlinear relationship deviates from the concentration-dependency correction applied by the instrument, $\delta_{c\text{-corrected}}(c_{raw})$ in Eq. (4), as shown in Fig. 4.

Here, the instrument internal concentration-dependency correction is shown for the used gas tank ambient after an offset correction at a concentration of 400 ppm, which is similar to the instrument's internal "referencing".

Thus, the mean deviations of the measured δ values from the concentration-dependency correction (top panel of Fig. 4) give an estimate of the uncertainty of measurements that is related to the deviation from the reference concentration. For

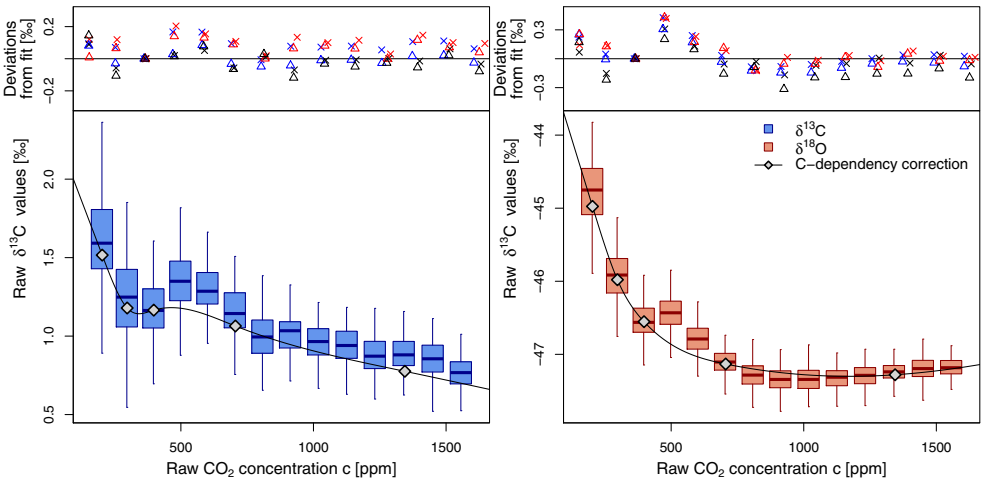

Figure 4. Box-and-whisker plots showing the nonlinear concentration dependency (c-dependency) of raw δ values for ^{13}C and ^{18}O respectively, here as an example for the CO_2 tank ambient. The measured c-dependency is compared to the respective c-dependency correction (black line, with grey symbols marking the data points used during the corresponding calibration measurement). The c-dependency correction is offset corrected to match the raw δ values at 400 ppm, and the mean deviation from the offset-corrected fit is shown in the top panel for two measurements (different symbols) with three different gas tanks (ambient in blue, bio in black and bio2 in red).

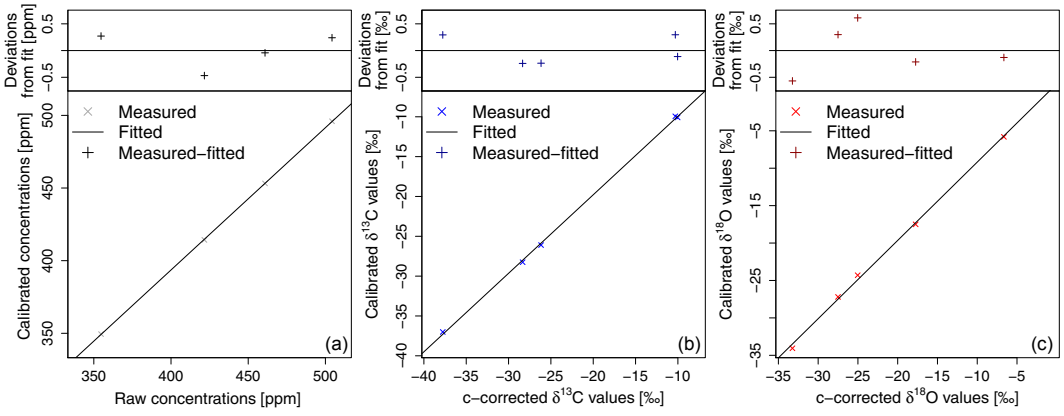

Figure 5. Linear calibrations for concentration **(a)** and concentration-corrected $\delta^{13}C$ and $\delta^{18}O$ **(b, c)** respectively.

referencing at 400 ppm, these deviations were approximately below 0.2 ‰ for ^{13}C and 0.4 ‰ for ^{18}O.

The measured linear relationships for concentration and δ scale calibration (Fig. 5) have R^2 values of above 0.9999 for concentrations, above 0.999 for δ ^{13}C and above 0.998 for δ ^{18}O. The linearity and potential accuracy, as defined by Tuzson et al. (2008), can be quantified as the 1σ standard deviation from the linear fits. The so defined potential accuracy of the instrument internal linear calibrations is 0.45 ppm for CO_2 concentration, 0.24 ‰ for $\delta^{13}C$ and 0.3 ‰ for $\delta^{18}O$. For both δ values, this is comparable to the uncertainty related to the nonlinear concentration calibration that varies with δ and c as discussed above.

The repeatability of the calibration curves is discussed here based on measurements of the nonlinear concentration dependency (Fig. 4) and repeated measurements of gas tanks with two different c and δ values to evaluate temporal changes in the respective linear relationships (Fig. 5). These measurements were taken every 6 h for a period of 9 days. For these repeated measurements the standard deviation of the calibrated values was below 0.2 ppm for concentrations and (if delta values were measured at 400 ppm and referenced at 380 ppm) below 0.05 and 0.1 ‰ for ^{13}C and ^{18}O respectively. Thus, the uncertainty related to the repeatability of the linear calibrations is smaller than the potential accuracy discussed above. For δ values, these values are comparable to the repeatability reported by several authors and measured with other laser spectrometers (e.g., Sturm et al., 2012, 2013; Vogel et al., 2013). For concentrations, on the other hand, Sturm et al. (2013) reported a much smaller value of 0.03 ppm, based on more frequent calibration. In our setup, the concentration calibration is only performed once after

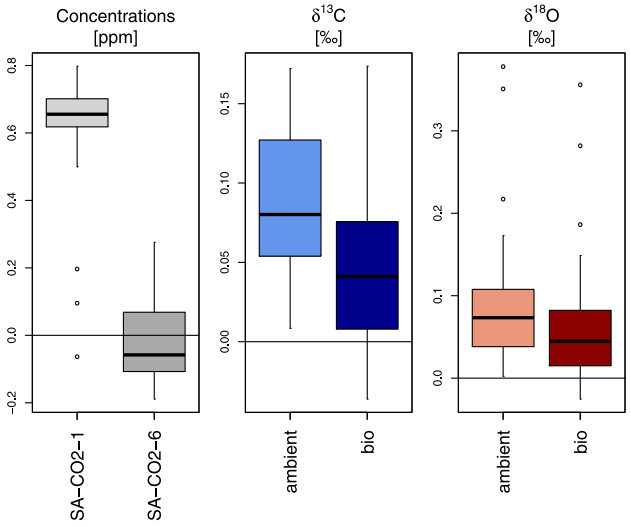

Figure 6. Box-and-whisker plots for the deviations of calibrated concentrations and δ values from laboratory measurements (at MPI in Jena) for repeated measurements of different calibration tanks (see Table 3 for c and δ values of the gas tanks) over a period of 9 days ($N = 36$). Delta values were measured at 400 ppm and "referencing" was done approximately every 30 min at 380 ppm to simulate conditions during a measurement campaign.

Table 6. Uncertainties related to the different calibration steps and their repeatability, defined as 1σ standard deviation of the respective calibration step.

Calibration	$\delta^{13}C$ (‰)	$\delta^{18}O$ (‰)	c (ppm)
Linear calibrations	0.24	0.3	0.45
Corresponding repeatability	0.05	0.1	0.2
Correction of c-dependency	0.2	0.4	–
Corresponding repeatability	0.15	0.15	–

the instrument is restarted; thus, there might be a potential for better repeatability in concentration measurements with more frequent concentration calibration.

For δ values measured at concentrations that deviate further from the reference concentration (here 380 ppm), the repeatability also depends on concentration (Table 7). Repeated measurements of these deviations have standard deviations below 0.15 ‰ for both δ values for concentrations between 200 and 1600 ppm.

For concentration measurements, the uncertainty related to the linear calibration dominates the overall uncertainty, whereas the uncertainty of δ-value measurements depends on the setup, in particular on the "referencing". If measurements were carried out at the concentration used during "referencing", the accuracy would be limited by the linear calibrations and the corresponding repeatability (c.f Table 6). If measurements were carried out at concentrations that deviate from the "referencing" concentration, the accuracy would be limited by the actual concentration dependency that deviates from the instrument internal correction of concentration dependency (see Fig. 4 and Table 6). In this case, the accuracy could be further improved by applying a correction of the concentration dependency based on more points.

Table 7. Standard deviations σ of the measured (calibrated) δ values over a large concentration range based on 6-hourly lab measurements over a period of 9 days.

	$\sigma(\delta_{meas} - \delta_{tank})$ ‰			
Concentration ppm	ambient tank ^{13}C	ambient tank ^{18}O	bio tank ^{13}C	bio tank ^{18}O
202	0.07	0.14	0.09	0.13
396	0.04	0.05	0.08	0.08
600	0.09	0.08	0.12	0.12
807	0.08	0.08	0.11	0.11
1018	0.10	0.08	0.13	0.11
1232	0.12	0.09	0.13	0.11
1450	0.14	0.11	0.15	0.12
1664	0.14	0.11	0.14	0.12
3145	0.17	0.15	0.17	0.15

3.1.3 Repeatability during the field campaign

We analyzed the repeatability of the Delta Ray analyzer under field conditions by evaluating half-hourly measurements of the same gas tank (SA-CO_2-5) during the whole measurement period. We use the standard deviations of measured concentrations and delta values to quantify the repeatability of our setup in the field including our calibration strategy. The standard deviations of these long-term measurements were below 0.3 ppm for CO_2 concentration, below 0.2 ‰ for $\delta^{13}C$ and below 0.25 ‰ for $\delta^{18}O$ (frequency distributions and time series of the long-term measurements are shown with color-coded metadata in Fig. 7. [2] For concentrations, the measured repeatability of approximately 0.3 ppm is slightly larger than the repeatability of the concentration calibration discussed above, but still below the potential accuracy discussed in Sect. 3.1.2. In the case of δ values, the obtained repeatability of approximately 0.2 ‰ for ^{13}C and 0.25 ‰ for ^{18}O is larger than the repeatability of the linear calibration parameters obtained during lab measurements (0.05 ‰ for ^{13}C and 0.1 ‰ for ^{18}O). The measured repeatability during the field campaign also exceeds the repeatability

[2] In the case of ^{13}C, we excluded the target measurements between 23 and 29 September, because we obtained a problem with the ^{13}C calibration that led to a large jump in the δ ^{13}C value of the (very depleted) target standard. This jump did not occur in the height measurements, probably because they were much closer to the reference δ value.

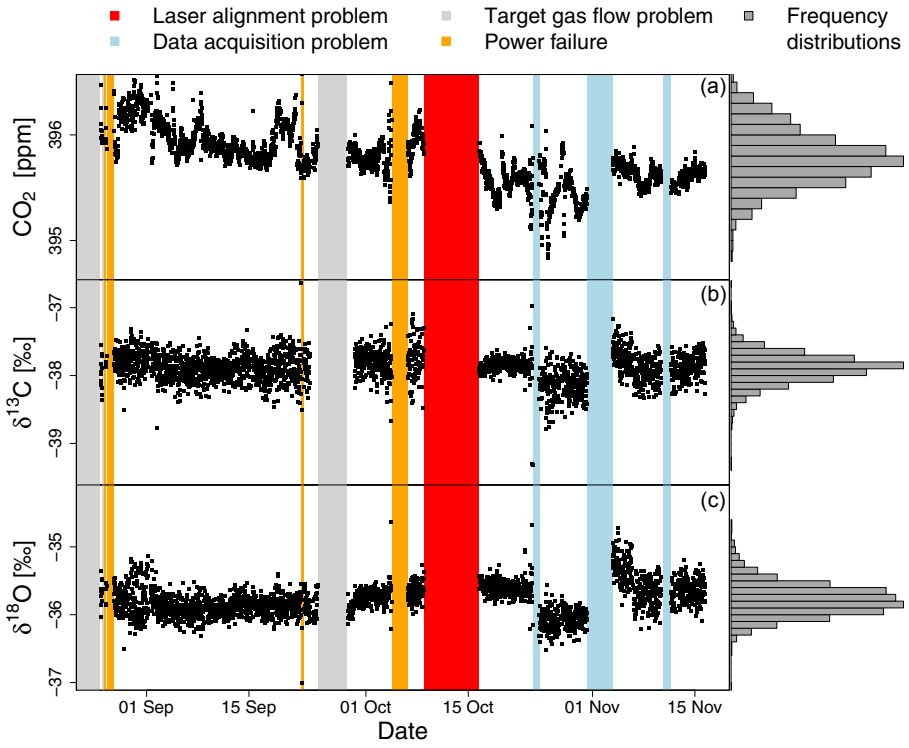

Figure 7. Time series and frequency distributions of half-hourly measurements of the concentration **(a)** and δ values **(b, c)** for target gas SA-CO_2-5 (see Table 3) for the whole measurement period excluding periods that show problems with target gas flow, calibration and laser alignment. The major reasons for data gaps are marked with different colors.

of the measurements of the concentration dependency (below 0.15 ‰ for both δ values over a large concentration range; see Sect. 3.1.2). This could be related to the fact that the δ values of our target standard were out of the calibration range, leading to an enhancement of fluctuations in the calibration parameters.

3.1.4 Response time

We measured the response time of our system (tubing and measurement cell of the Delta Ray analyzer) by using the valve system shown in Fig. 2 to switch from ambient air with $\delta^{13}C \approx -9$ and $\delta^{18}O \approx 1$ ‰ to tank air with $\delta^{13}C \approx -38$ and $\delta^{18}O \approx -36$ ‰. The time series of the measured δ values after the change of the valve position (Fig. 8) consisted of three different phases that can be related to different physical processes: for the first phase, the measured δ values remained constant for $\tau_1 \approx 14$ s. This is the setup-specific time it took for the gas to flush the tubes and valves before entering the cell. For the second phase, we observed a quadratic decay of the measured δ values, which we relate to mixing of gas within the tubes (before it enters the cell). This phase dominated the temporal response of our system for $\tau_2 \approx 4.5$ s. The third phase of temporal response is the exponential decay with a characteristic decay time (defined here using the 10 % threshold) $\tau_{10\,\%} \approx 10$ s for $\delta^{13}C$ and $\tau_{10\,\%} \approx 11$ s for $\delta^{18}O$. This exponential behavior can be derived for an idealized situation that includes perfect mixing in a volume V_{mix} yielding

$$\tau_{10\,\%} = \frac{\log(10) \cdot p_{cell} \cdot V_{mix}}{\Phi},$$

with flow rate Φ, cell pressure p_{cell} and effective mixing volume V_{mix}. Using the volume of the measurement cell as an upper threshold for the effective mixing volume within the cell, $\max(V_{mix}) = V_{cell} = 80$ mL, we can calculate an upper threshold for $\tau_{10\,\%}$. With the instruments flow rate of $\Phi = 0.08$ slpm and the cell pressure of $p_{cell} \approx 100$ mbar, we get $\tau_{10\,\%,max} \approx 13.6$ s. Thus, the measured value of $\tau_{10\,\%}$ is slightly below this value, indicating $V_{mix} < V_{cell}$. We define the total response time τ_{tot} as the time span it took until the step change between the two inlets reached 0.1 % of the corresponding difference in δ values, with $\tau_3 = \tau_{0.1\,\%} = 3 \cdot \tau_{10\,\%}$. The three different phases of instrument response (tube transport τ_1, tube-mixing-dominated change τ_2 and cell-mixing-dominated change τ_3) summed up to a net response time $\tau_{tot} = \tau_1 + \tau_2 + \tau_3 < 60$ s. Thus, the cell flushing time of our application (60 s) is appropriate to produce independent measurements of two different inlets.

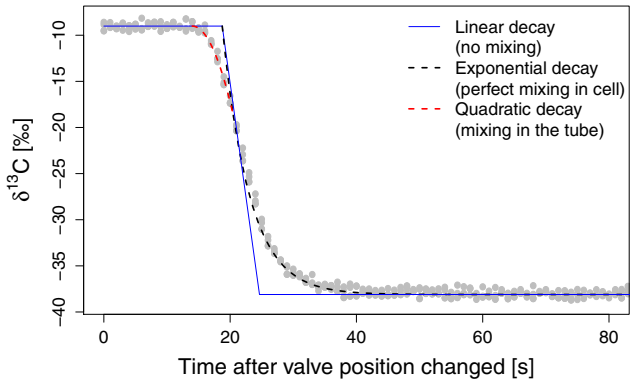

Figure 8. The response time of our experimental setup can be divided into three phases with different dominant mechanisms: directly after switching, it took approximately 14 s to flush the tubing, the adjacent 4 s were dominated by the mixing processes in the tubes before the gas entered the measuring cell (quadratic fit) and finally we observed a response behavior that is dominated by mixing processes within the measuring cell (exponential fit) with a characteristic decay time of $\tau_{10\,\%} = 10$ s for $\delta^{13}C$. These response times were similar for $\delta^{18}O$ (not shown). The linear fit shown here describes a first order approximation of the theoretical cell response for the (unrealistic) assumption that there is no mixing in the measurement cell. From this assumption, it can be derived that the δ values would show a dominantly linear decay with the slope $m = (\delta_{new} - \delta_{old})/\tau_{theoretical}$ and the theoretical instrument cell response time $\tau_{theoretical} = p \times V/\Phi$, with pressure p, Volume V and flow rate Φ. In our case $\delta_{new} - \delta_{old} = -29\,‰$ and thus $\tau_{theoretical} = 5.9$ s.

3.1.5 Utilization rate, power consumption and maintenance effort

We define the utilization rate as the number of successfully recorded measurement cycles divided by the number of measurement cycles that were theoretically possible during the field campaign (approximately 4200). This can be calculated separately for (a) profile measurements and (b) target gas measurements, because some data gaps were specific for target measurements. The utilization rate was approximately 80 % for measurements of the height profile and approximately 70 % for target gas measurements. Two major reasons for data gaps reduced the utilization rate for both profile and target measurement by 8.6 % (a laser alignment problem that was resolved after 7 days) and 6 % (three data acquisition problems, the longest lasting 3 days). Additionally, four external power supply problems at the field site lead to a further reduction of the utilization rate by 3.3 %. These data gaps, as well as smaller data gaps, that reduced the utilization rate are listed in Table 8. In the case of target measurements, the main reason for data gaps (accounting for a reduction of the utilization rate of more than 9 %) was plumbing issues that led to a contamination of the target gas by ambient air. Thus, a more stable target plumbing would be a promising approach to increase the utilization rate, as well as a more stable power supply and more frequent field trips.

Table 8. Percentage of total measurement time for major data gaps. The latter two data gaps concerned only target gas measurements.

Reason for data gap	Percentage
Data acquisition problems	6.0 %
Laser alignment problem	8.6 %
Calibration	1.5 %
Power failures	3.3 %
Additional measurements	1.6 %
Plumbing issues (only target)	9.5 %
Switching unit failure (only target)	0.7 %

Maintenance effort and power consumption of the whole setup were moderate: the analyzer's power consumption of approximately 220 W was slightly smaller than the power consumption of the basic infrastructure of the setup that included the pump to purge the nine inlet tubes and the heated valve box (330 W). To maintain and to control the setup, we went to the field site weekly or every 2 weeks and used remote access to the instrument via a satellite connection.

3.2 Ecological application

3.2.1 Time series of measured quantities

The measured CO_2 concentrations at 45 m height at our field site in a managed beech forest in central Germany ranged from 385 to 450 ppm, with corresponding δ values between -11 and $-7\,‰$ for ^{13}C and between -6 and $2\,‰$ for ^{18}O over a 3-month period in autumn 2015 (Fig. 9). As the lower heights commonly contain larger amounts of respired CO_2 with a typically lighter carbon and oxygen composition, the lower inlets show larger CO_2 concentrations c with smaller δ values. We calculated a 3-month time series of nighttime Keeling plot intercepts $\delta^{13}C_{KP}$ and $\delta^{18}O_{KP}$ that can be interpreted as the respective isotopic composition of nighttime net ecosystem CO_2 exchange (respiration) $R^{13}_{eco}C$ and $R^{18}_{eco}O$ (shown with temperature and precipitation data in Fig. 10). A particular feature of the measurement period is an early snow and frost event with negative temperatures during four nights between 11 and 15 October 2015 (Fig. 10). The corresponding snow event on 13 October was visible on a canopy picture taken at midday on 13 October 2015. The time of the snow and frost event coincided with changes in the characteristics of $\delta^{18}O$, $R^{18}_{eco}O$ and $R^{13}_{eco}C$. For $\delta^{18}O$ and $R^{18}_{eco}O$ a strong decrease was obtained after the snow event. This decrease was the largest signal in the respective time series. For $R^{13}_{eco}C$, the analysis of its potential meteorological drivers yielded different results for the time periods before and after the first snow. Additionally, according to eddy covariance measurements, the forest was a net CO_2 sink with negative diurnal net ecosystem exchange (NEE) before 12 October (with only

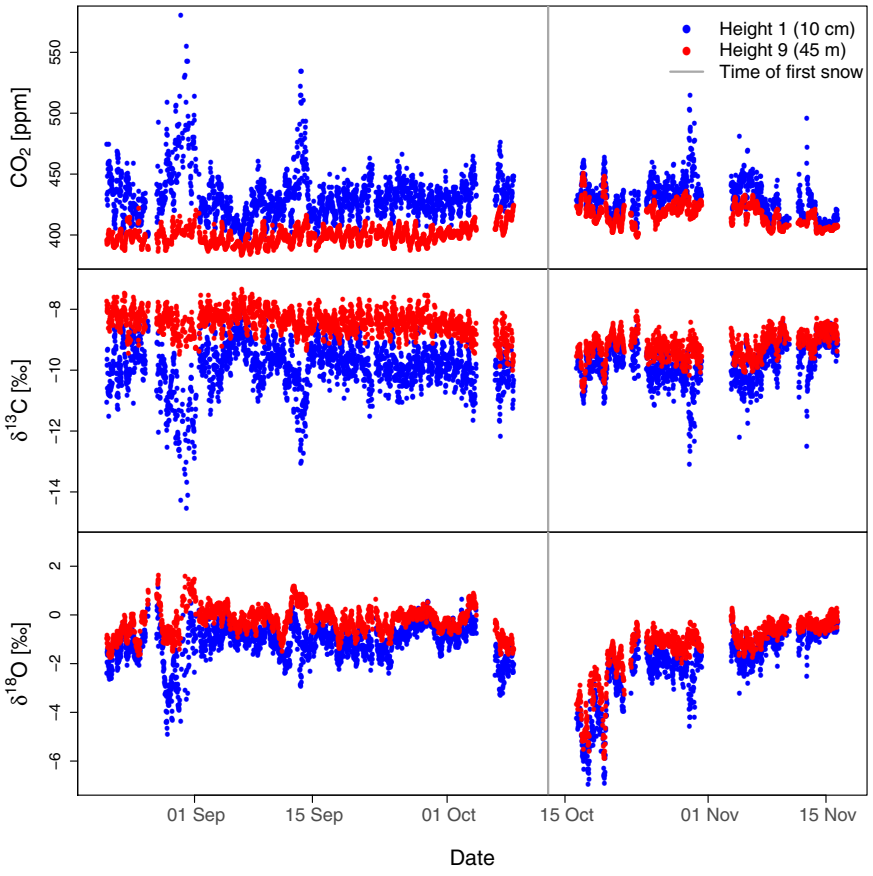

Figure 9. Time series of all measured concentrations c and both δ values at the lowest (blue points) and highest (red points) inlet at 0.1 and 45 m height respectively.

one exception), whereas it was a net CO_2 source with positive diurnal NEE after the snow event on 13 October (also with only one exception).

3.2.2 Potential drivers for $R^{13}_{eco}C$

Previous studies linked the temporal variability of the ^{13}C composition of ecosystem respiration $R^{13}_{eco}C$ partially to changes in the meteorological conditions during photosynthesis, namely relative humidity (RH), vapor pressure deficit (VPD), photosynthetically active radiation (PAR) and the ratio VPD / PAR (Ekblad and Högberg, 2001; Bowling et al., 2002; Knohl et al., 2005). These links occurred with time lags that correspond to the time lag between assimilation and respiration, which is approximately 4 to 5 days for mature trees (Kuzyakov and Gavrichkova, 2010). The observed time-lagged links between meteorological variables and $R^{13}_{eco}C$ were interpreted by the respective authors as an indication for a link between the isotopic composition of respiration $R^{13}_{eco}C$ and the isotopic composition of recent assimilates $\delta^{13}C_{Ass}$, which is controlled by photosynthetic discrimination of the heavier ^{13}C according to the Farquhar model (Farquhar et al., 1989). Thus, in accordance with previous studies, we hypothesize the following:

Hypothesis A. The variability of $R^{13}_{eco}C$ can be partly explained by the isotopic composition of recent assimilates $\delta^{13}C_{Ass}$, which is controlled by meteorological drivers during photosynthesis according to the Farquhar model. Thus, the variability of $R^{13}_{eco}C$ is linked to the variability of meteorological drivers of photosynthesis and photosynthetic discrimination with a time lag that is consistent with the time lag between respiration and assimilation.

To test this hypothesis, we calculated the Pearson correlation coefficient r_{pear} between $R^{13}_{eco}C$ and the n-day sum (with n from 1 to 6) of the meteorological quantities that we expect to control ^{13}C discrimination for different time shifts τ. For the time period before the first snow (when the ecosystem was a CO_2 sink), the strongest correlation we found was a moderate negative correlation between $R^{13}_{eco}C$ and the 2-day sum of net radiation R_n with a time shift τ of 2 days (Fig. 11). This correlation is significant with a Pearson correlation coefficient r_{pear} of approximately -0.56, which is clearly beyond the corresponding critical value of approximately ± 0.38 for $N = 45$ and $\alpha = 0.005$. The time lag of this correlation is in accordance with the expected time lag

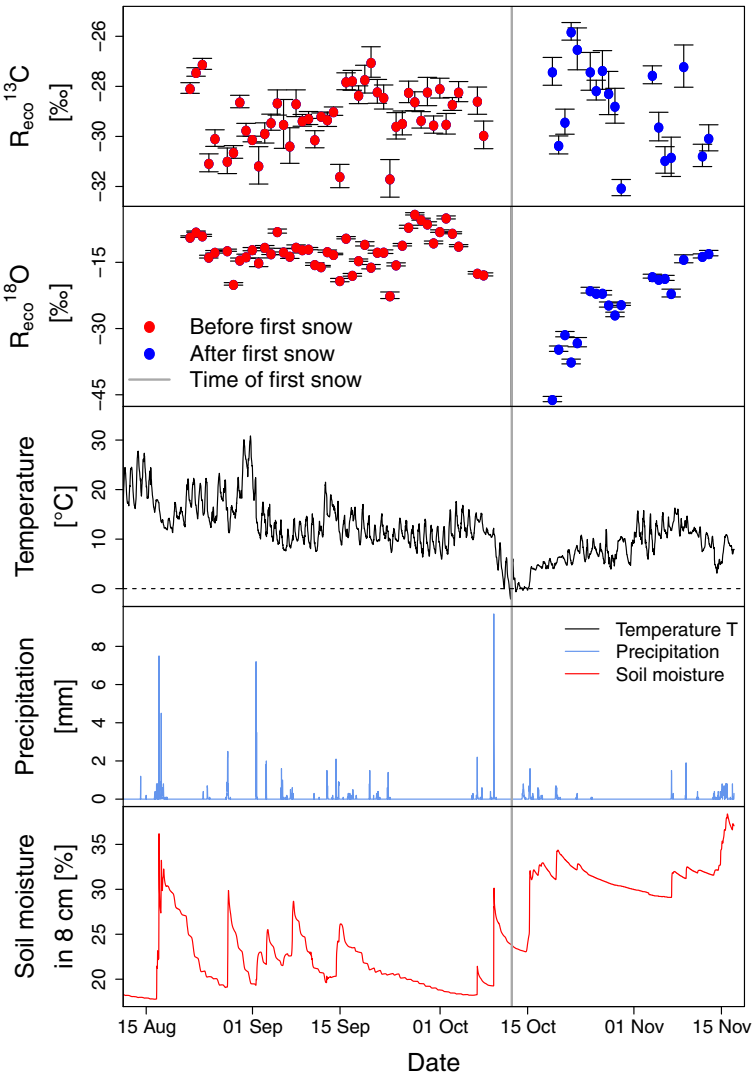

Figure 10. Time series of the measured isotopic composition of nighttime CO_2 exchange (respiration) $R^{13}_{eco}C$ and $R^{18}_{eco}O$ based on Keeling plot intercepts in combination with temperature, precipitation and soil moisture in 8 cm depth. Error bars denote the standard error of the Keeling plot intercept (based on the linear regression of δ vs. $1/c$). A particular feature of this time series is a first snow and frost event on 13 October 2015, marked in gray.

between assimilation and respiration of 2 to 5 days for mature trees (Kuzyakov and Gavrichkova, 2010). However, the correlation itself cannot be directly explained by the Farquhar model of discrimination as radiation influences both the CO_2 supply (by influencing stomatal conductance) and the CO_2 demand (by influencing assimilation) in the leaf (Farquhar and Sharkey, 1982). In particular we did not find a significant time-lagged positive correlation between $R^{13}_{eco}C$ and VPD, RH or the ratio VPD / PAR (Fig. 11), which could be directly associated with the Farquhar model and has been found by the above-mentioned studies. To test if it might still be reasonable to interpret the observed negative correlation of $R^{13}_{eco}C$ with R_n as a time-lagged link between $R^{13}_{eco}C$ and the isotopic composition of recently assimilated material $\delta^{13}C_{Ass}$ on an ecosystem scale, we performed a more complex calculation of $\delta^{13}C_{Ass}$ by using the multilayer model CANVEG (see Sect. 2.9). The advantage of CANVEG is that it accounts for the nonlinear interactions between air temperature, air humidity, radiation, stomatal conductance and photosynthesis. Before the first snow event during our measurement period, the modeled $\delta^{13}C_{Ass}$ correlated significantly with the diurnal sum of net radiation R_n with an r_{pear} of 0.89 (Fig. 12) – corresponding $r_{crit} \approx 0.33$ for $N = 63$. However, in contrast to the time-lagged correlation, which we found in our Keeling plot data, this correlation is positive (Fig. 12). As the multilayer model does not support the interpretation of the observed negative correlation between R_n and $R^{13}_{eco}C$

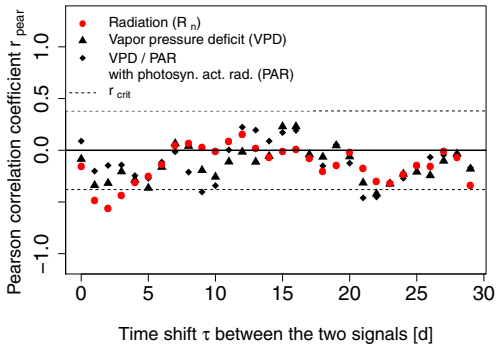

Figure 11. Pearson correlation coefficient of the isotopic composition of ecosystem respiration $R^{13}_{eco}C$ and the 2-day sum of different meteorological variables (shifted by different times τ) before the first snow event in autumn 2015.

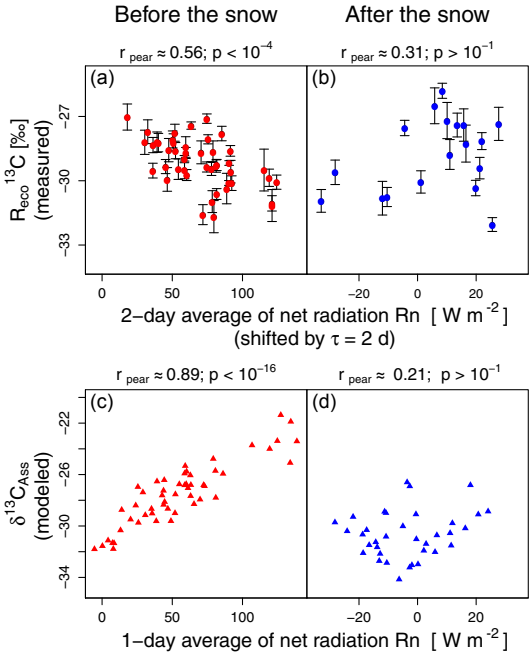

Figure 12. Observed relationships between net radiation R_n, the measured isotopic composition of ecosystem respiration $R^{13}_{eco}C$ **(a, b)** and the modeled ^{13}C composition of assimilated material $\delta^{13}C_{Ass}$ **(c, d)**. Significant correlations were observed before the first snow **(a, c)** but became insignificant after the snow **(b, d)**. r_{pear} and p values are derived from the respective linear regressions.

through the variability of the isotopic composition of recent assimilates $\delta^{13}C_{Ass}$, it does not support hypothesis A.

An alternative interpretation of the observed correlation between the isotopic composition of respiration $R^{13}_{eco}C$ and net radiation R_n would be a link between $R^{13}_{eco}C$ and the amount of recent assimilates (alternatively to the isotopic composition of recent assimilates). Because soil respiration has been measured to account for around 80 % of ecosystem respiration in an old beech forest at less than a 30 km distance to our field site (Knohl et al., 2008), we assume that soil respiration dominates ecosystem respiration and thus we further focus on soil respiration and discuss the following hypothesis:

Hypothesis B. The observed time-lagged correlation between $R^{13}_{eco}C$ and net radiation R_n is related to the temporal variability of the ratio of autotrophic to total soil respiration[3].

A link between photosynthesis and autotrophic soil respiration has been shown in many studies throughout different ecosystems, including a beech-dominated forest at less than a 30 km air-line distance to our field site in a managed beech forest (Moyano et al., 2008). In this study, the authors found that 73 % of the variability in rhizosphere respiration (the major part of autotrophic soil respiration) correlated with photosynthesis (GPP) and the ratio between autotrophic and total soil respiration was approximately 50 %. Additionally, evidences for a large temporal variability on diurnal and seasonal scales of the contribution of autotrophic to total soil respiration have been reported for a temperate hardwood forest (Savage et al., 2013) and for a mature temperate boreal forest (Carbone et al., 2016).

In our field experiment, the observed correlation between $R^{13}_{eco}C$ and R_n with an r_{pear} of 0.56 (and thus $r^2_{pear} = 0.3$) links 30 % of the variability of $R^{13}_{eco}C$ to R_n, with a time lag of 2–4 days. As the measured isotopic composition of ecosystem respiration $R^{13}_{eco}C$ spanned a range of 6 ‰, this corresponds to a range of 1.8 %. Hypothesis B would further imply that this variability over a range of 1.8 ‰ corresponds to that proportion of the variability of autotrophic respiration that is linked to photosynthesis. If we were to estimate this proportion to represent 73 % of the total variability of autotrophic respiration (following Moyano et al., 2008), the corresponding total variability of autotrophic respiration would correspond to a range of approximately 2.5 ‰. If in autumn the ratio of autotrophic to total respiration would approximate 0 %, this value of 2.5 ‰ would be equal to the difference $\Delta_{tot\text{-}aut} = \delta_{tot} - \delta_{aut}$ between the isotopic composition of total respiration δ_{tot} and the isotopic composition of autotrophic respiration δ_{aut}. In general, a value of $\Delta_{tot\text{-}aut} = +2.5$ ‰ is within the range of differences that have been reviewed to be on average about +4 ‰ (Bowling et al., 2008) for different ecosystems. A positive value of $\Delta_{tot\text{-}aut}$ with a lighter $\delta^{13}C$ composition of autotrophic respiration would be consistent with hypothesis B. As a note of caution, however, not a single on of the studies that analyze autotrophic soil respiration in the above-mentioned review was performed in a forest ecosystem. For C3 woody species, including forests, more enriched $\delta^{13}C$ values of autotrophic soil respiration, and thus negative values for $\Delta_{tot\text{-}aut}$, have been reported (Ghashghaie

[3]The term "autotrophic" is not consistently defined among different authors. Here we use this term as equivalent to "root-derived respiration", including respiration from the living root tissue, from microorganisms in the rhizosphere and mycorrhizal symbiotic fungi.

and Badeck, 2014). In a beech forest in southern Germany, the sign of some involved fractionation effects varied temporally (Paya et al., 2016). Thus, the comparison with literature data about the temporal variability of the ratio between autotrophic and total soil respiration and the respective isotopic compositions gives the possibility that hypothesis B is true, but we cannot, however, prove it without additional independent measurements. To test this hypothesis, we would need to measure the amount and the isotopic composition of autotrophic respiration, total soil respiration and ecosystem respiration (e.g., by a trenching experiment) at our field site with an appropriate time resolution to capture the day-to-day variability during the field campaign. Lab measurements using incubations could also give an idea of the isotopic composition of autotrophic and total soil respiration but would not fully reflect field site conditions.

3.2.3 Characteristics of $R^{18}_{eco}O$ and $\delta^{18}O$

The seasonal variability of $\delta^{18}O$ and $R^{18}_{eco}O$ (shown in Figs. 9 and 10) is influenced by oxygen exchange when CO_2 gets dissolved in different water pools (e.g., leaf and soil water) with variable isotopic compositions. These isotopic compositions in turn are controlled by multiple physical and biological factors such as temperature, precipitation, vapor pressure deficit or the activity of the enzyme carbonic anhydrase that accelerates the oxygen exchange between water and CO_2 (Miller et al., 1999; Farquhar et al., 1993; Gillon and Yakir, 2000; Bowling et al., 2003a; Wingate et al., 2009). The strongest feature of the measured time series of $R^{18}_{eco}O$ is an approximately 30 ‰ large decrease within 10 days from approximately −18 ‰ on 7 October to approximately −46 ‰ on 18 October (Fig. 10). During the same time period, the $\delta^{18}O$ value of nighttime ambient CO_2 at 45 m height decreased from approximately −1 down to −3.5 ‰ at nighttime and down to −6 ‰ during daytime (Fig. 9). As for $R^{18}_{eco}O$, this decrease is the strongest signal in the measured time series of $\delta^{18}O$. The time of these decreases in $R^{18}_{eco}O$ and $\delta^{18}O$ coincided with the time of the first snow and frost event in autumn 2015. This indicates that the snow event has a noticeable effect on both $\delta^{18}O$ and $R^{18}_{eco}O$, but as the change in (nighttime) $R^{18}_{eco}O$ is more than 10 times larger than the corresponding change in $\delta^{18}O$ of nighttime CO_2, this effect is particularly enhanced for $R^{18}_{eco}O$. For comparison, similar strong peaks in $R^{18}_{eco}O$ have been observed in a semiarid woodland after precipitation in New Mexico (Shim et al., 2013), but this study refers to a monsoon-dominated ecosystem with comparably large variability in the ^{18}O and does not focus on the difference of these pulses of snow and rain events.

Possible explanations for the observed large decreases in both $\delta^{18}O$ and $R^{18}_{eco}O$ after the snow would involve the ^{18}O exchange of CO_2 with water pools that are fed by the recent snow event and the response to changes in many of the above-mentioned physical and biological factors that influence the oxygen exchange between CO_2 and water. One of the factors that can cause a depletion in ^{18}O due to the exchange of oxygen between CO_2 and snow-fed water pools is the fact that snow has in general a lighter ^{18}O composition than rain. The isotopic composition of rain can often be related to Rayleigh fractionation processes (Gat, 1996) and is thus related to isotopic exchange between the raindrops and air masses in clouds when rain is falling (Gat, 1996; Bolin, 1959; Friedman et al., 1962). As a result of the continuous isotopic exchange with air masses in the cloud, raindrops do not carry the very depleted isotopic composition within the cloud, whereas for snow, the isotopic exchange between the falling snowflakes and the air masses in the cloud does not take place, resulting in a more depleted precipitation (Gat, 1996). For example, Orlowski et al. (2016) reported a maximal difference of approximately 15.5 ‰ between the $\delta^{18}O$ values of rain and snow over a 2-year measurement period at a field site at an approximately 160 km air-line distance from our field site. A smaller maximal difference of approximately 9 ‰ between the $\delta^{18}O$ of snow and the corresponding monthly means for rain was reported by Wenninger et al. (2011), based on 2 years of measurements at two catchments in a German black forest at a 414 km air-line distance from our field site. Thus, the ^{18}O-depleted isotopic composition of snow compared to rain may explain some of the observed 30 ‰ decrease in $R^{18}_{eco}O$. One possible additional effect could be the fact that soil-respired CO_2 is typically in equilibrium not with rain but with soil water in the top soil layers (0 to 20 cm; Miller et al., 1999; Wingate et al., 2009). Evaporative effects can shift the isotopic composition in the upper soil layers towards more ^{18}O-enriched values (Miller et al., 1999; Wingate et al., 2009), potentially increasing the $\delta^{18}O$ difference before and after the snow event.

We tested the correlation between $R^{18}_{eco}O$ and different meteorological variables that potentially control the isotopic composition of different water pools within the ecosystem over the whole measurement period as well as the subperiods before and after the first snow (Table 9). As the underlying multiple interaction processes between oxygen in CO_2 and different water pools, as well as the respective isotopic compositions of these pools, are complex, this analysis was not performed to causally link the measured $R^{18}_{eco}O$ to a single meteorological driver but rather to look for changes of these correlations that could be interpreted as changes in the processes that drive $R^{18}_{eco}O$ before and after the snow event. For the whole measurement period, the strongest of the analyzed correlations was a correlation between $R^{18}_{eco}O$ and soil moisture at a depth of 8 cm with an R^2 of 0.49 and $p < 10^{-9}$. As this correlation becomes insignificant when it is calculated for the periods before and after the snow separately, it can be related to the strong decrease in $R^{18}_{eco}O$ after the snow event that correlates to a rise in soil moisture when the snow melts (Fig. 10). This would be consistent with a heavier ^{18}O composition in the top soil layers (due to evaporation) before the snow, yielding also higher $\delta^{18}O$ values of $R^{18}_{eco}O$. Additionally, other variables that correlated significantly with

Table 9. R^2 values for correlations between the ^{18}O composition of nighttime CO_2 exchange $R^{18}_{eco}O$ and different meteorological variables. Significance thresholds are given by *** for $p < 10^{-4}$, ** for $p < 10^{-3}$ and * for $p < 10^{-2}$. For some parameters the height above the ground (with negative values indicating the depth below the ground) is given in brackets; the parameters without such indication are measured 42 m above the ground.

	All periods		Before the snow		After the snow	
Soil moisture (−8 cm)	0.49	***	0.04		0.00	
Upwards shortwave radiation	0.40	***	0.28	*	0.04	
VPD	0.18	**	0.09		0.22	
Soil temperature (−8 to −64 cm)	0.36	***	0.06		0.70	***
Air temperature	0.22	**	0.02		0.61	**
Air temperature (2 m)	0.21	**	0.05		0.60	**
Upwards longwave radiation	0.20	**	0.02		0.61	**
Incoming longwave radiation	0.05		0.49	***	0.03	
Ambient pressure	0.05		0.39	***	0.36	*
Incoming shortwave radiation	0.39	***	0.23	**	0.13	
Dew point temperature	0.02		0.38	***	0.14	
Specific humidity	0.02		0.34	***	0.17	
H_2O concentration	0.02		0.34	***	0.17	
Actual vapor pressure	0.02		0.33	***	0.18	
Relative humidity	0.28	***	0.31	***	0.15	
Rain	0.01		0.28	**	0.05	

$R^{18}_{eco}O$ during the whole measurement period such as soil and air temperatures or shortwave radiation (Table 9) are related to soil evaporation. For the sub-periods before and after the first snow, we found multiple significant correlations with meteorological drivers such as soil and air temperatures, pressure or actual vapor pressure (Table 9). The significant correlations before the first snow become insignificant (or less significant) after the snow and vice versa. This behavior indicates a difference in the processes that drive the ^{18}O isotopic composition of nighttime net ecosystem CO_2 exchange $R^{18}_{eco}O$ before and after the snow event.

4 Conclusions

Field-applicable instruments to analyze the isotopic composition of CO_2 have a large potential to be useful for long-term measurement setups on meteorological towers and networks such as ICOS (https://www.icos-ri.eu/) or NEON (http://www.neonscience.org/) to deliver new insights into the carbon cycle. The new isotope ratio infrared spectrometer Delta Ray used in this study provides an opportunity to measure the CO_2 concentration c and its isotopic compositions $\delta^{13}C$ and $\delta^{18}O$ with limited maintenance effort at remote sites. Here, we evaluate the instrument internal calibration and demonstrate the field applicability of the Delta Ray IRIS, which we used to measure c, $\delta^{13}C$ and $\delta^{18}O$ in a managed beech forest for 3 months in autumn 2015. The Delta Ray IRIS implemented here with the instrument's internal calibration showed adequate precision, accuracy and repeatability to perform robust measurements of c, $\delta^{13}C$ and $\delta^{18}O$ in air in our continuous setup. For measurements of δ values at concentrations that deviate from the "referencing" concentration, the uncertainty is dominated by the instrument internal correction of concentration dependency and improvements in the accuracy could potentially be achieved by more detailed analysis of this concentration dependency. The easy operation of the automatically calibrated Delta Ray IRIS allowed us to measure seasonal variability of the isotopic composition of nighttime CO_2 exchange based on Keeling plots. The strong effect of the first frost and snow event on both the $\delta^{13}C$ and $\delta^{18}O$ of nighttime CO_2 exchange indicates that singular events, even if short, may strongly influence the isotopic imprint of terrestrial ecosystems on atmospheric CO_2.

Code and data availability. An earlier version of the multilayer model CANVEG can be found at https://nature.berkeley.edu/biometlab/BiometWeb/canoak_V2.c. All data used for the figures presented here are provided in the Supplement.

Appendix A: Measures to improve data quality

To reduce the uncertainty of the calculated isotopic composition of nighttime CO_2 exchange (respiration) $R^{13}_{eco}C$ and $R^{18}_{eco}O$, we used the following approaches concerning setup and post-processing.

- *Minimizing the sampling time.* One of the key assumptions of the Keeling plot approach in Eq. (1) is the mixing of a constant background with one (integrated) source. This assumption is justified if there is no significant change in the background concentration c_{bg}, its isotopic composition δ_{bg} and the isotopic composition of the (integrated) source δ_s for all data points that are taken into account for a single Keeling plot. For the case of an integrated source, a constant δ_s can be ensured when the isotopic composition of the individual source components $\delta_{s,i}$ and the relative contribution of the individual source components α_i in Eq. (2) are constant. As all these quantities ($\delta_{s,i}$, α_i, c_{bg} and δ_{bg}) can vary with time, this assumption tends to be violated more often for longer measurement times. Thus, the uncertainty of calculated Keeling plot intercepts can be reduced by minimizing the measurement time, as discussed, for example, by Bowling et al. (2003b), who only recommend the use of measurements that took less than 5 h for analyzing Keeling plot intercepts for $\delta^{18}O$. As our setup measured all of the nine heights within 30 min, we were able to calculate Keeling plots for shorter periods. During data analysis we calculated Keeling plots on timescales between 30 min and 5 h.

- *Increasing the CO_2 concentration range.* The linear regression that underlies the Keeling plot can be improved significantly by increasing the CO_2 concentration (Zobitz et al., 2006). In our setup, we increase the CO_2 concentration range by using data from all nine inlet heights within one Keeling plot, but this, on the other hand, could violate the assumption of constant relative contributions of the individual source components α_i in Eq. (2) to the integrated source. To analyze whether there is any bias (which may have several contributions) due to the inclusion of the different inlet positions, we evaluated the Keeling plots for the lower inlets (heights 1–4) and for all inlets (heights 1–9) separately. The difference Δ between the these Keeling plot intercepts based on different data sets showed a symmetric frequency distribution around 0 (Fig. S1 in the Supplement). By including all heights into the data analysis, we reduced the error of the intercept σ from a mean value of $\overline{\sigma_{low}} \approx 1.5‰$ to $\overline{\sigma_{all}} \approx 0.8‰$ for both isotopic species. These numbers refer to Keeling plots that include data from three consecutive measurement cycles, yielding a temporal resolution of 90 min. Reasons for the choice of this time resolution are given below.

- *Performing an ordinary Model I regression instead of a Model II regression.* We used an ordinary Model I regression instead of a Model II regression. According to Zobitz et al. (2006), this approach takes into account that the error of the measured δ values dominates over the error of the measured concentrations and yields unbiased estimates of the Keeling plot intercept. In our setup, the application of a Model I regression can be justified by the fact that the relative precision of δ measurements is more than an order of magnitude larger than the relative precision of the CO_2 concentration measurements: to estimate the relative precision of the three measured quantities, we calculated the ratio of the Allan deviation at our measurement time of 20 s over the typical range of c, $\delta^{13}C$ and $\delta^{18}O$. We further define the typical range as the median of the ranges that were obtained during the 30 min measurement cycles. Thus, with the Allan deviations in Table 5 and with typical ranges of 26 ppm, 1.5 and 1.1 ‰ for c, $\delta^{13}C$ and $\delta^{18}O$, the relative precision for the obtained variability in CO_2, $\delta^{13}C$ and $\delta^{18}O$ is on the order of 10^{-3}, 10^{-2} and 10^{-1} respectively. Thus, the relative precision of the concentration measurement is at least an order of magnitude better than the relative precision of δ measurements.

- *Filtering data to get only high quality linear regressions.* Data filtering to remove bad quality and biased (Model II) linear regressions has been often done by excluding data with a to low CO_2 concentration range (Pataki et al., 2003; Bowling et al., 2005). Whereas Pataki et al. (2003) recommended the exclusion of all data from the analysis that spans a CO_2 range below 75 ppm, Bowling et al. (2005) chose this threshold to be 40 ppm. This data filtering approach, based on CO_2 concentration range, does not seem necessary when applying a Model I regression: Zobitz et al. (2006) analyzed consequences of small CO_2 concentration ranges numerically as well as analytically and concluded that for Keeling plot intercepts based on Model I regressions (1) a bias at low CO_2 concentration ranges is not expected at current analytical error levels and (2) that errors in the intercept can be small, even for small CO_2 concentration ranges, if the δ values are measured accurately enough. Figure S2 shows the relationship between the CO_2 concentration range and the standard error of the intercept σ for a measurement period of 30 min. This figure also shows two comparable approaches for data filtering that accept 85 % of the data: one approach would be to directly remove data with large intercept errors and the other approach, as mentioned above, would be to remove data with a too-low CO_2 range. As is visible in Fig. S2, this approach would remove considerable amounts of data with a very small standard error of the intercept σ, which might be good quality data. For this reason (and as we do not expect

a bias occurring for small CO_2 concentration ranges for our Model-I-type regression), we decide on a direct filtering based on a σ threshold. We filtered out data with σ values larger than the 85th percentile of all σ's. The filtered nighttime Keeling plot intercepts based on 90 min of data acquisition had R^2 values with a median of 0.87 and 0.81 for ^{13}C and ^{18}O, with mean values of 0.85 and 0.77 and standard deviations σ of 0.1 and 0.16 respectively. Example Keeling plots with R^2 values spanning the range of mean $\pm 1\sigma$ are provided in Fig. S5.

– *Removing outliers.* Our setup, based on the measurement of $\delta^{13}C$, $\delta^{18}O$ and CO_2 concentration c, enabled us to calculate individual Keeling plots based on all inlet heights (heights 1–9) with a temporal resolution of 30 min. We calculated Keeling plots on different timescales ranging from 30 min to 5 h by using 1 to 10 measurement cycles and evaluated how the Keeling plot intercepts $\delta^{13}C_{KP}$ and the corresponding standard errors of the linear regression σ changed (Fig. S3). Additionally, the calculation of Keeling plot intercepts based on longer timescales increased the number of Keeling plot intercepts within reasonable ranges. For Keeling plots that were averaged over 2 h (5 h), a fraction of 97 % (99 %) of the Keeling Plot intercepts was between −33 and −25 ‰. Because the range of the Keeling plot intercepts should not depend on the chosen timescale, we considered the Keeling plot intercepts that were outside of this range as outliers and removed them from further analysis (also for Keeling plot intercepts that were based on shorter timescales).

– *Choosing a time resolution for individual Keeling plots.* To decide on a suitable time resolution to analyze the temporal variability of the Keeling plot intercepts, we had to solve the trade-off between (1) more accurate data on longer timescales and (2) a larger number of data points that were available (after the above-mentioned filtering procedures). We decided to fit the individual Keeling Plots on 90 min resolution, which yields a maximal number of $N_{filtered} \approx 2300$ accepted data points and a median of 0.76 ‰ for the standard errors σ (Fig. S4).

– *Calculation of weighted means for nighttime data.* For analyzing variations in the nighttime CO_2 exchange (respiration) R_{eco} on seasonal timescales we used the (filtered) individual Keeling plots, each based on 90 min of input data, and calculated the mean over all Keeling plots that were collected between 21:30 and 02:30 LT (local winter time, GMT+1; using the weight w based on the standard error σ of the Keeling plot intercept: $w = 1/\sigma^2$).

The Supplement related to this article is available online at https://doi.org/10.5194/amt-10-4537-2017-supplement.

Author contributions. The authors contributed to this paper in the following ways: the experimental setup and data processing were carried out, discussed and interpreted by JB-B and AK. The validation of and simulations with the multilayer model CANVEG (Sect. 2.9) were performed, discussed and interpreted by YY, JB-B and AK. All authors proof-read and commented on the paper.

Competing interests. We declare that we have no conflict of interest. However, we borrowed the instrument at no cost from Thermo Scientific, Waltham, USA, to perform instrument tests and to use the instrument under field conditions. Additionally, we were able to perform lab measurements to evaluate the calibration strategy at the facility of Thermo Scientific in Bremen at no cost. Jelka Braden-Behrens and Alexander Knohl published a short (not peer reviewed) technical paper (Braden-Behrens et al., 2017) together with Hans-Jürg Jost and Magda Mandic, who were both working for Thermo Scientific, when we borrowed the instrument. This not-peer-reviewed technical paper also briefly describes our experimental setup and discusses instrument performance.

Acknowledgements. This project was partly funded by the Dorothea-Schlözer Fellowship and by the German Research Foundation (DFG, project ISOFLUXES KN 582/7-1). The work was partially supported by the European Research Council under the European Union's Horizon 2020 research and innovation programme (grant agreement no. 682512 – OXYFLUX). We thank Thermo Scientific, Waltham, USA, for lending us the instrument for free and for making it possible for us to perform additional measurements in the lab. We particularly thank Hans-Jürg Jost, Magda Mandic and Danijela Smajgl for their advice and support, especially concerning how to set up, calibrate and operate the Delta Ray analyzer. The technicians of the bioclimatology group of the University of Göttingen, especially Dietmar Fellert, Frank Tiedemann and Edgar Tunsch, as well as the student assistant Elke Schäpermeier, helped substantially with the experimental setup and maintenance. We thank Yakov Kuzyakov, Lydia Gentsch and Mattia Bonazza for their remarks on data interpretation. Additionally, we thank the forest manager Ulrich Breitenstein for allowing the experimental setup at this site.

This open-access publication was funded by the University of Göttingen.

Edited by: Frank Keppler
Reviewed by: three anonymous referees

References

Affek, H. and Yakir, D.: The stable isotopic composition of atmospheric CO_2, in: Treatise on geochemistry, edited by: Holland, H. and Turekian, K., 5, 2 Edn., 179–212, Elsevier, https://doi.org/10.1016/B978-0-08-095975-7.00407-1, 2014.

Anthoni, P., Knohl, A., Rebmann, C., Freibauer, A., Mund, M., Ziegler, W., Kolle, O., and Schulze, E. D.: Forest and agricultural land-use-dependent CO_2 exchange in Thuringia, Germany, Glob. Change Biol., 10, 2005–2019, https://doi.org/10.1111/j.1365-2486.2004.00863.x, 2004.

Baldocchi, D. D.: Measuring and modelling carbon dioxide and water vapour exchange over a temperate broad-leaved forest during the 1995 summer drought, Plant Cell Environ., 20, 1108–1122, https://doi.org/10.1046/j.1365-3040.1997.d01-147.x, 1997.

Baldocchi, D. D. and Bowling, D. R.: Modelling the discrimination of $^{13}CO_2$ above and within a temperate broad-leaved forest canopy on hourly to seasonal time scales, Plant Cell Environ., 26, 231–244, https://doi.org/10.1046/j.1365-3040.2003.00953.x, 2003.

Baldocchi, D. D. and Wilson, K. B.: Modelling CO_2 and water vapor exchange of a temperate broadleaved forest across hourly to decadal time scales, Ecol. Model., 142, 155–184, https://doi.org/10.1016/S0304-3800(01)00287-3, 2001.

Baldocchi, D. D., Vogel, C. A., and Hall, B.: Seasonal variation of carbon dioxide exchange rates above and below a boreal jack pine forest, Agr. Forest Meteorol., 83, 147–170, https://doi.org/10.1016/S0168-1923(96)02335-0, 1997.

Baldocchi, D. D., Fuentes, J. D., Bowling, D. R., Turnipseed, A. A., and Monson, R. K.: Scaling isoprene fluxes from leaves to canopies: Test cases over a boreal aspen and a mixed species temperate forest, J. Appl. Meteorol., 38, 885–898, https://doi.org/10.1175/1520-0450(1999)038<0885:SIFFLT>2.0.CO;2, 1999.

Baldocchi, D. D., Wilson, K. B., and Gu, L.: How the environment, canopy structure and canopy physiological functioning influence carbon, water and energy fluxes of a temperate broad-leaved deciduous forest – An assessment with the biophysical model CANOAK., Tree Physiol., 22, 1065–1077, https://doi.org/10.1093/treephys/22.15-16.1065, 2002.

Ballantyne, A. P., Miller, J. B., Baker, I. T., Tans, P. P., and White, J. W. C.: Novel applications of carbon isotopes in atmospheric CO_2: What can atmospheric measurements teach us about processes in the biosphere?, Biogeosciences, 8, 3093–3106, https://doi.org/10.5194/bg-8-3093-2011, 2011.

Barbour, M. M., Hunt, J. E., Kodama, N., Laubach, J., McSeveny, T. M., Rogers, G. N. D., Tcherkez, G., and Wingate, L.: Rapid changes in $\delta^{13}C$ of ecosystem-respired CO_2 after sunset are consistent with transient ^{13}C enrichment of leaf respired CO_2, New Phytol., 190, 990–1002, https://doi.org/10.1111/j.1469-8137.2010.03635.x, 2011.

Bolin, B.: On the use of tritium as a tracer for water in nature, in: Proceedings of the 2nd conference on the peaceful uses of atomic energy, UN, Geneva, 18336–1844, 1959.

Bowling, D. R., Tans, P. P., and Monson, R. K.: Partitioning net ecosystem carbon exchange with isotopic fluxes of CO_2, Glob. Change Biol., 7, 127–145, https://doi.org/10.1046/j.1365-2486.2001.00400.x, 2001.

Bowling, D. R., McDowell, N. G., Bond, B. J., Law, B. E., and Ehleringer, J. R.: ^{13}C content of ecosystem respiration is linked to precipitation and vapor pressure deficit, Oecologia, 131, 113–124, https://doi.org/10.1007/s00442-001-0851-y, 2002.

Bowling, D. R., McDowell, N. G., Welker, J. M., Bond, B. J., Law, B. E., and Ehleringer, J. R.: Oxygen isotope content of CO_2 in nocturnal ecosystem respiration: 2. Short-term dynamics of foliar and soil component fluxes in an old-growth ponderosa pine forest, Global Biogeochem. Cy., 17, GB2082, https://doi.org/10.1029/2003GB002082, 2003a.

Bowling, D. R., McDowell, N. G., Welker, J. M., Bond, B. J., Law, B. E., and Ehleringer, J. R.: Oxygen isotope content of CO_2 in nocturnal ecosystem respiration: 1. Observations in forests along a precipitation transect in Oregon, USA, Global Biogeochem. Cy., 17, 3101–3114, https://doi.org/10.1029/2003GB002081, 2003b.

Bowling, D. R., Sargent, S. D., Tanner, B. D., and Ehleringer, J. R.: Tunable diode laser absorption spectroscopy for stable isotope studies of ecosystem-atmosphere CO_2 exchange, Agr. Forest Meteorol., 118, 1–19, https://doi.org/10.1016/S0168-1923(03)00074-1, 2003c.

Bowling, D. R., Burns, S. P., Conway, T. J., Monson, R. K., and White, J. W. C.: Extensive observations of CO_2 carbon isotope content in and above a high-elevation subalpine forest, Global Biogeochem. Cy., 19, GB3023, https://doi.org/10.1029/2004GB002394, 2005.

Bowling, D. R., Pataki, D. E., and Randerson, J. T.: Carbon isotopes in terrestrial ecosystem pools and CO_2 fluxes, New Phytol., 178, 24–40, https://doi.org/10.1111/j.1469-8137.2007.02342.x, 2008.

Braden-Behrens, J., Knohl, A., Jost, H.-J., and Mandic, M.: Measuring the isotopic composition of ecosystem respiration in a temperate beech forest, Thermo Sci. White Pap., WP30385, http://tools.thermofisher.com/content/sfs/brochures/WP-30385-IRIS-Isotopic, last access: 15 November 2017.

Carbone, M. S., Richardson, A. D., Chen, M., Davidson, E. A., Hughes, H., Savage, K. E., and Hollinger, D. Y.: Constrained partitioning of autotrophic and heterotrophic respiration reduces model uncertainties of forest ecosystem carbon fluxes but not stocks, J. Geophys. Res.-Biogeo., 121, 2476–2492, https://doi.org/10.1002/2016JG003386, 2016.

Coplen, T. B.: Guidelines and recommended terms for expression of stable-isotope-ratio and gas-ratio measurement results, Rapid Commun. Mass Sp., 25, 2538–2560, https://doi.org/10.1002/rcm.5129, 2011.

Ekblad, A. and Högberg, P.: Natural abundance of ^{13}C in CO_2 respired from forest soils reveals speed of link between tree photosynthesis and root respiration, Oecologia, 127, 305–308, https://doi.org/10.1007/s004420100667, 2001.

Esler, M. B., Griffith, D. W. T., Wilson, S. R., and Steele, L. P.: Precision trace gas analysis by FT-IR spectroscopy. 2. The $^{13}C/^{12}C$ isotope ratio of CO_2, Anal. Chem., 72, 216–221, https://doi.org/10.1021/ac990563x, 2000.

Farquhar, G. D. and Sharkey, T. D.: Stomatal conductance and photosynthesis, Annu. Rev. Plant Physio., 33, 317–345, https://doi.org/10.1146/annurev.pp.33.060182.001533, 1982.

Farquhar, G. D., Ehleringer, J. R., and Hubick, K. T.: Carbon isotope discrimination and photosynthesis, Annu. Rev. Plant Phys., 40, 503–537, https://doi.org/10.1146/annurev.pp.40.060189.002443, 1989.

Farquhar, G. D., Lloyd, J., Taylor, J. A., Flanagan, L. B., Syvertsen, J. P., Hubick, K. T., Wong, S. C., and Ehleringer, J. R.: Vegetation effects on the isotope composition of oxygen in atmospheric CO_2, Nature, 363, 439–443, https://doi.org/10.1038/363439a0, 1993.

Flanagan, L. B. and Ehleringer, J. R.: Ecosystem-atmosphere CO_2 exchange: interpreting signals of change using stable isotope ratios, Trends Ecol. Evol., 13, 10–14, https://doi.org/10.1016/S0169-5347(97)01275-5, 1998.

Friedman, I., Machta, L., and Soller, R.: Water-vapor exchange between a water droplet and its environment, J. Geophys. Res., 67, 2761–2766, https://doi.org/10.1029/JZ067i007p02761, 1962.

Gat, J. R.: Oxygen and hydrogen isotopes in the hydrologic cycle, Annu. Rev. Earth Pl. Sc., 24, 225–262, https://doi.org/10.1146/annurev.earth.24.1.225, 1996.

Geldern, R. V., Nowak, M. E., Zimmer, M., Szizybalski, A., Myrttinen, A., Barth, J. A. C., and Jost, H.-J.: Field-based stable isotope analysis of carbon dioxide by mid-infrared laser spectroscopy for carbon capture and storage monitoring, Anal. Chem., 86, 12191–12198, https://doi.org/10.1021/ac5031732, 2014.

Gemery, P. A., Trolier, M., and White, J. W. C.: Oxygen isotope exchange between carbon dioxide and water following atmospheric sampling using glass flasks, J. Geophys. Res., 101, 14415–14420, https://doi.org/10.1029/96JD00053, 1996.

Ghashghaie, J. and Badeck, F. W.: Opposite carbon isotope discrimination during dark respiration in leaves versus roots – a review, New Phytol., 201, 751–769, https://doi.org/10.1111/nph.12563, 2014.

Gillon, J. S. and Yakir, D.: Naturally low carbonic anhydrase activity in C_4 and C_3 plants limits discrimination against $C^{18}OO$ during photosynthesis, Plant Cell Environ., 23, 201–213, https://doi.org/10.1046/j.1365-3040.2000.00597.x, 2000.

Griffis, T. J.: Tracing the flow of carbon dioxide and water vapor between the biosphere and atmosphere: A review of optical isotope techniques and their application, Agr. Forest Meteorol., 174–175, 85–109, https://doi.org/10.1016/j.agrformet.2013.02.009, 2013.

Griffith, D. W. T., Deutscher, N. M., Caldow, C., Kettlewell, G., Riggenbach, M., and Hammer, S.: A Fourier transform infrared trace gas and isotope analyser for atmospheric applications, Atmos. Meas. Tech., 5, 2481–2498, https://doi.org/10.5194/amt-5-2481-2012, 2012.

Guillon, S., Pili, E., and Agrinier, P.: Using a laser-based CO_2 carbon isotope analyser to investigate gas transfer in geological media, Appl. Phys. B-Lasers O., 107, 449–457, https://doi.org/10.1007/s00340-012-4942-8, 2012.

International Atomic Energy Agency: Reference and intercomparison materials for stable isotopes of light elements, in: Proceedings of a consultants meeting, edited by: IAEA, IAEA–TECDOC–825, Vienna, 1995.

Keeling, C. D.: The concentration and isotopic abundances of atmospheric carbon dioxide in rural areas, Geochim. Cosmochim. Ac., 13, 322–334, https://doi.org/10.1016/0016-7037(58)90033-4, 1958.

Kerstel, E. and Gianfrani, L.: Advances in laser-based isotope ratio measurements: Selected applications, Appl. Phys. B-Lasers O., 92, 439–449, https://doi.org/10.1007/s00340-008-3128-x, 2008.

Knohl, A. and Baldocchi, D. D.: Effects of diffuse radiation on canopy gas exchange processes in a forest ecosystem, J. Geophys. Res., 113, G02023, https://doi.org/10.1029/2007JG000663, 2008.

Knohl, A. and Buchmann, N.: Partitioning the net CO_2 flux of a deciduous forest into respiration and assimilation using sta-

ble carbon isotopes, Global Biogeochem. Cy., 19, GB4008, https://doi.org/10.1029/2004GB002301, 2005.

Knohl, A., Werner, R. A., Geilmann, H., and Brand, W. A.: Kel-F^{TM} discs improve storage time of canopy air samples in 10-mL vials for CO_2-$\delta^{13}C$ analysis, Rapid Commun. Mass Sp., 18, 1663–1665, https://doi.org/10.1002/rcm.1528, 2004.

Knohl, A., Werner, R. A., Brand, W. A., and Buchmann, N.: Short-term variations in ^{13}C of ecosystem respiration reveals link between assimilation and respiration in a deciduous forest, Oecologia, 142, 70–82, https://doi.org/10.1007/s00442-004-1702-4, 2005.

Knohl, A., Søe, A. R. B., Kutsch, W. L., Göckede, M., and Buchmann, N.: Representative estimates of soil and ecosystem respiration in an old beech forest, Plant Soil, 302, 189–202, https://doi.org/10.1007/s11104-007-9467-2, 2008.

Kuzyakov, Y. and Gavrichkova, O.: Review: Time lag between photosynthesis and carbon dioxide efflux from soil: A review of mechanisms and controls, Glob. Change Biol., 16, 3386–3406, https://doi.org/10.1111/j.1365-2486.2010.02179.x, 2010.

Miller, J. B., Yakir, D., White, J. W. C., and Tansl, P. P.: Measurement of $^{18}O/^{16}O$ in the soil-atmosphere CO_2 flux, Global Biogeochem. Cy., 13, 761–774, https://doi.org/10.1029/1999GB900028, 1999.

Mohn, J., Werner, R. A., Buchmann, B., and Emmenegger, L.: High-precision $\delta^{13}CO_2$ analysis by FTIR spectroscopy using a novel calibration strategy, J. Mol. Struct., 834–836, 95–101, https://doi.org/10.1016/j.molstruc.2006.09.024, 2007.

Mohn, J., Zeeman, M. J., Werner, R. A., Eugster, W., and Emmenegger, L.: Continuous field measurements of delta ^{13}C-CO_2 and trace gases by FTIR spectroscopy, Isot. Environ. Healt. S., 44, 241–51, https://doi.org/10.1080/10256010802309731, 2008.

Moyano, F. E., Kutsch, W. L., and Rebmann, C.: Soil respiration fluxes in relation to photosynthetic activity in broad-leaf and needle-leaf forest stands, Agr. Forest Meteorol., 148, 135–143, https://doi.org/10.1016/j.agrformet.2007.09.006, 2008.

Mund, M.: Carbon pools of European beech forests (Fagus sylvatica) under different silvicultural management, Berichte des Forschungszentrums Waldökosysteme Reihe A, Band, 189, 1–256, 2004.

Ogée, J., Peylin, P., Ciais, P., Bariac, T., Brunet, Y., Berbigier, P., Roche, C., Richard, P., Bardoux, G., and Bonnefond, J.-M.: Partitioning net ecosystem carbon exchange into net assimilation and respiration using $^{13}CO_2$ measurements: A cost-effective sampling strategy, Global Biogeochem. Cy., 17, 3901–3916, https://doi.org/10.1029/2002GB001995, 2003.

Oikawa, P., Sturtevant, C., Knox, S. H., Verfaillie, J., Huang, Y.-W., and Baldocchi, D. D.: Revisiting the Partitioning of Net Ecosystem Exchange of CO_2 into Photosynthesis and Respiration with Simultaneous Flux Measurements of $^{13}CO_2$ and CO_2, Soil Respiration and a Biophysical Model, CANVEG, Agr. Forest Meteorol., 234–235, 149–163, https://doi.org/10.1016/j.agrformet.2016.12.016, 2017.

Orlowski, N., Kraft, P., Pferdmenges, J., and Breuer, L.: Exploring water cycle dynamics by sampling multiple stable water isotope pools in a developed landscape in Germany, Hydrol. Earth Syst. Sc., 20, 3873–3894, https://doi.org/10.5194/hess-20-3873-2016, 2016.

Pataki, D. E., Ehleringer, J. R., Flanagan, L. B., Yakir, D., Bowling, D. R., Still, C., Buchmann, N., Kaplan, J. O., and Berry, J. A.: The application and interpretation of Keeling plots in terrestrial carbon cycle research, Global Biogeochem. Cy., 17, 1022, https://doi.org/10.1029/2001GB001850, 2003.

Paya, A. M., Grams, T. E. E., and Bauerle, T. L.: Seasonal dynamics of $\delta^{13}C$ of C-rich fractions from Picea abies (Norway spruce) and Fagus sylvatica (European beech) fine roots, Plant Cell Environ., 39, 2004–2013, https://doi.org/10.1111/pce.12765, 2016.

Savage, K., Davidson, E. A., and Tang, J.: Diel patterns of autotrophic and heterotrophic respiration among phenological stages, Glob. Change Biol., 19, 1151–1159, https://doi.org/10.1111/gcb.12108, 2013.

Schnyder, H., Schäufele, R., and Wenzel, R.: Mobile, outdoor continuous-flow isotope-ratio mass spectrometer system for automated high-frequency ^{13}C- and ^{18}O-CO_2 analysis for Keeling plot applications, Rapid Commun. Mass Sp., 18, 3068–3074, https://doi.org/10.1002/rcm.1731, 2004.

Shim, J. H., Powers, H. H., Meyer, C. W., Knohl, A., Dawson, T. E., Riley, W. J., Pockman, W. T., and McDowell, N.: Hydrologic control of the oxygen isotope ratio of ecosystem respiration in a semi-arid woodland, Biogeosciences, 10, 4937–4956, https://doi.org/10.5194/bg-10-4937-2013, 2013.

Sturm, P., Eugster, W., and Knohl, A.: Eddy covariance measurements of CO_2 isotopologues with a quantum cascade laser absorption spectrometer, Agr. Forest Meteorol., 152, 73–82, https://doi.org/10.1016/j.agrformet.2011.09.007, 2012.

Sturm, P., Tuzson, B., Henne, S., and Emmenegger, L.: Tracking isotopic signatures of CO_2 at the high altitude site Jungfraujoch with laser spectroscopy: Analytical improvements and representative results, Atmos. Meas. Tech., 6, 1659–1671, https://doi.org/10.5194/amt-6-1659-2013, 2013.

Thermo Fisher Scientific: Delta Ray^{TM} Isotope ratio infrared spectrometer: Operating manual, Thermo Scientific, Bremen, 2014.

Thomson, J. J.: Rays of positive electricity, Nature, 79, 52–56, https://doi.org/10.1038/079052a0, 1908.

Tuzson, B., Mohn, J., Zeeman, M. J., Werner, R. A., Eugster, W., Zahniser, M. S., Nelson, D. D., McManus, J. B., and Emmenegger, L.: High precision and continuous field measurements of $\delta^{13}C$ and $\delta^{18}O$ in carbon dioxide with a cryogen-free QCLAS, Appl. Phys. B-Lasers O., 92, 451–458, https://doi.org/10.1007/s00340-008-3085-4, 2008.

Vardag, S. N., Hammer, S., Sabasch, M., Griffith, D. W. T., and Levin, I.: First continuous measurements of $\delta^{18}O$-CO_2 in air with a Fourier transform infrared spectrometer, Atmos. Meas. Tech., 8, 579–592, https://doi.org/10.5194/amt-8-579-2015, 2015.

Vogel, F. R., Huang, L., Ernst, D., Giroux, L., Racki, S., and Worthy, D. E. J.: Evaluation of a cavity ring-down spectrometer for in situ observations of $^{13}CO_2$, Atmos. Meas. Tech., 6, 301–308, https://doi.org/10.5194/amt-6-301-2013, 2013.

Wehr, R., Munger, J., Nelson, D., McManus, J., Zahniser, M., Wofsy, S., and Saleska, S.: Long-term eddy covariance measurements of the isotopic composition of the ecosystem-atmosphere exchange of CO_2 in a temperate forest, Agr. Forest Meteorol., 181, 69–84, https://doi.org/10.1016/j.agrformet.2013.07.002, 2013.

Wehr, R., Munger, J. W., McManus, J. B., Nelson, D. D., Zahniser, M. S., Davidson, E. A., Wofsy, S. C., and Saleska, S. R.: Seasonality of temperate forest photosynthesis and daytime respira-

tion, Nature, 534, 680–683, https://doi.org/10.1038/nature17966, 2016.

Wendeberg, M., Richter, J. M., Rothe, M., and Brand, W. A.: Jena Reference Air Set (JRAS): A multi-point scale anchor for isotope measurements of CO_2 in air, Atmos. Meas. Tech., 6, 817–822, https://doi.org/10.5194/amt-6-817-2013, 2013.

Wenninger, J., Koeninger, P., and Schneider, P.: Isotopic characterization of snow variability in two mountainous catchments, black forest mountains, Germany, in: International symposium on water resource and environmental protection (ISWREP), 1004–1007, 2011.

Werle, P. W.: Diode-laser sensors for in-situ gas analysis, in: Laser in environmental and life sciences: Modern analytical methods, edited by: Hering, P., Lay, J. P., and Stry, S., Springer, Berlin, Heidelberg, 223–243, https://doi.org/10.1007/978-3-662-08255-3_11, 2004.

Werner, C., Schnyder, H., Cuntz, M., Keitel, C., Zeeman, M. J., Dawson, T. E., Badeck, F. W., Brugnoli, E., Ghashghaie, J., Grams, T. E. E., Kayler, Z. E., Lakatos, M., Lee, X., Máguas, C., Ogée, J., Rascher, K. G., Siegwolf, R. T. W., Unger, S., Welker, J. M., Wingate, L., and Gessler, A.: Progress and challenges in using stable isotopes to trace plant carbon and water relations across scales, Biogeosciences, 9, 3083–3111, https://doi.org/10.5194/bg-9-3083-2012, 2012.

Wingate, L., Ogée, J., Cuntz, M., Genty, B., Reiter, I., Seibt, U., Yakir, D., Maseyk, K., Pendall, E. G., Barbour, M. M., Mortazavi, B., Burlett, R., Peylin, P., Miller, J., Mencuccini, M., Shim, J. H., Hunt, J., and Grace, J.: The impact of soil microorganisms on the global budget of $\delta^{18}O$ in atmospheric CO_2, P. Natl. Acad. Sci. USA, 106, 22411–22415, https://doi.org/10.1073/pnas.0905210106, 2009.

Yakir, D. and Sternberg, L. D. S. L.: The use of stable isotopes to study ecosystem gas exchange, Oecologia, 123, 297–311, https://doi.org/10.1007/s004420051016, 2000.

Yakir, D. and Wang, X.-F.: Fluxes of CO_2 and water between terrestrial vegetation and the atmosphere estimated from isotope measurements, Nature, 380, 515–517, https://doi.org/10.1038/380515a0, 1996.

Zhang, J., Griffis, T. J., and Baker, J. M.: Using continuous stable isotope measurements to partition net ecosystem CO_2 exchange, Plant Cell Environ., 29, 483–496, https://doi.org/10.1111/j.1365-3040.2005.01425.x, 2006.

Zobitz, J., Keener, J., Schnyder, H., and Bowling, D. R.: Sensitivity analysis and quantification of uncertainty for isotopic mixing relationships in carbon cycle research, Agr. Forest Meteorol., 136, 56–75, https://doi.org/10.1016/j.agrformet.2006.01.003, 2006.